Advances in multicore optical fibres for endoscopy

Roper, James

Award date:
2016

Awarding institution:
University of Bath

ADVANCES IN MULTICORE OPTICAL FIBRES FOR ENDOSCOPY

James Crawford Roper

A thesis submitted for the degree of Doctor of Philosophy

University of Bath

Department of Physics

October 2015

for Grandpa

Contents

Acknowledgements

Firstly, my family. Mum, Dad and Zimus, thank you for all the support (also financial) over the many years at Bath.

All those currently in the CPPM (and a number whom have left) for making my time in the department such an enjoyable and pleasant place to be.

I'd like to particularly thank:

Fei and Brian who took the time to teach me the dark art of fibre fabrication.

Gareth, Lucy, Itan and Jim for their patience in answering questions and giving explanations, often repeatedly.

I'd also like to single out Jamie for assisting me with that early-early morning fibre draw, let's not do that again.

Thanks also go to the physics football team for a 'much needed' distraction on Friday afternoons; that victory in 2012 will live long in the memory.

And lastly, Jonathan. You got me through it!

Overview

This thesis presents advances in the fabrication and application of multicore optical fibres, specifically pertaining to nonlinear endomicroscopy. Chapters 1 and 2 present the necessary background material to understanding the results presented in chapters 3 and 4.

Through chapter 1 the properties of optical fibres are described. The basic structure of silica fibres and the parameters used to classify them are discussed. Typical methods of fabrication are outlined along with post fabrication processes. The experimental procedures required in the later stages of the thesis are also covered.

Chapter 2 introduces and reviews nonlinear endoscopy. Various nonlinear process involved are described and the current positions of each in the field of nonlinear imaging discussed.

In chapter 3 a method for minimising the variation in group indices of cores within a multicore fibre is outlined, experimentally examined and verified. The minimisation is achieved by specifically controlling the core diameters within the multicore fibre for a given wavelength.

The fourth chapter introduces a ‘proof of concept’ method for reducing the bend sensitivity of a multicore fibre. Here a helical path is followed by the cores within the fibre. The specific challenges of fabrication are also described.

Chapter 1

Optical Fibres

1.1 Description of step index optical fibres

Defining a step index optical fibre is done using the core-cladding refractive index contrast Δ and the normalised frequency known as the *V* parameter. The refractive index contrast is calculated by

$$\Delta = \frac{n_{co} - n_{cl}}{n_{co}} \tag{1.1}$$

the normalised frequency *V* is defined as

$$V = \frac{2\pi\rho}{\lambda}(n_{co}^2 - n_{cl}^2)^{\frac{1}{2}} \tag{1.2}$$

where λ is the wavelength and ρ is the core radius. In the case where $V < 2.405$ the optical fibres will support only one mode [1], the fundamental, this is known as a single mode fibre. Looking at equation 1.2 it can been seen that any step index optical fibre can be made to be single mode by increasing the wavelength of light. This means that through control of the core radius and refractive indices an optical fibre can be designed to be single mode for a specified wavelength. As the wavelength of a higher order mode increases it approaches a "cut-off" wavelength where the mode is no longer guided. As the mode approaches cut-off the field distribution spreads out and the mode becomes much more sensitive to

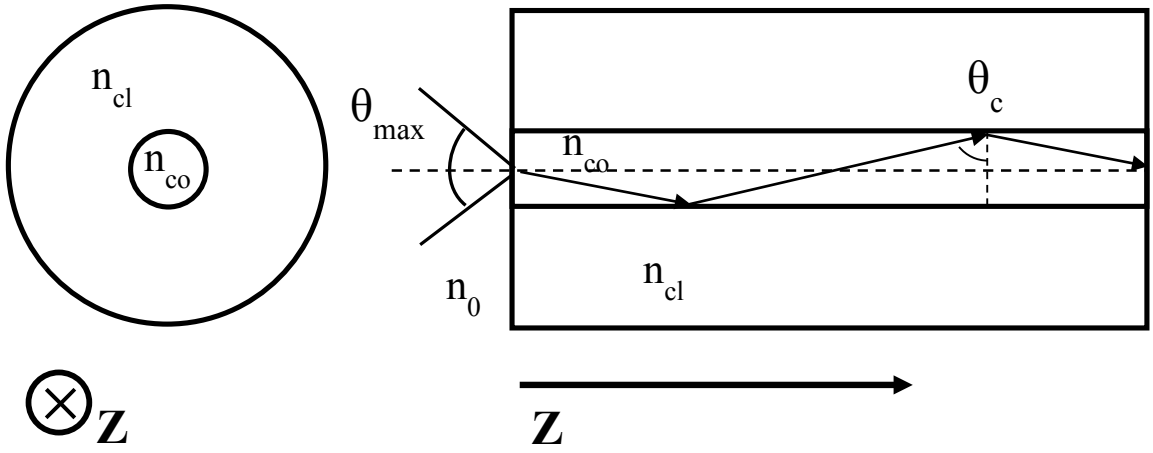

Figure 1.1: Step index fibre schematic showing the core-cladding boundary across the fibre face (left) and a geometric representation of a fibres numerical appature (left).

loss due to bending. The spreading out of the mode as it approaches cut-off also causes the effective index to vary significantly.

To successfully launch light into an optical fibre the incoming light must be within the acceptance angle of the fibre, figure 1.1, known as the numerical aperture (NA). For a given core-cladding index step it is given by

$$NA = \sin(\theta_{max}) = (n_{co}^2 - n_{cl}^2)^{\frac{1}{2}} \qquad (1.3)$$

where θ_{max} is the maximum acceptance angle of the fibre along the propagation axis. When coupling light between fibres the NA of each dictates the values of lenses required for best coupling.

1.2 Graded Index optical fibres

A graded index optical fibre contains, as the name suggests, a core of changing refractive index. Typically the refractive index will follow a parabola-like profile. The shape of the refractive index within the core is described by,

$$n(r) = n_{co}\left(1 - 2\Delta\left(\frac{r}{\alpha}\right)^{g}\right)^{\frac{1}{2}} \tag{1.4}$$

where n_{co} is the maximum refractive index within the core, α is the radius of the core region, $\Delta = (n_{co} - n_{cl})/n_{co}$, r is the radial distance from the centre of the fibre and g is the grade profile parameter. The grade profile parameter describes the shape of the graded index. As seen in figure 1.2 an infinite value for g would result in a step-index fibre and a g value of one would give a triangular profile. In most graded index fibres a value around two is used.

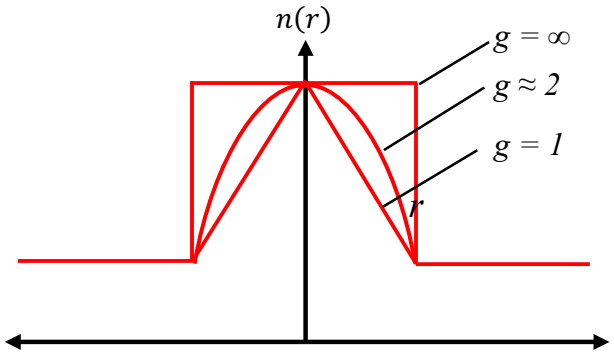

Figure 1.2: Refractive index profiles across the core of a graded index fibre as a result of changing g values.

It is possible to classify a graded index fibre in much the same way as conventional step index fibre. Assuming the weakly guiding case (where the difference between the maximum refractive index and the cladding is small), the mode field shape will have changed little when compared to an equivalent step index fibre. The main changes being a slight decrease in the peak amplitude of the field accompanied by an increase in the mode radius. The selection of

appropriate Bessel functions to describe the mode of the graded index fibre allows an equivalent step index fibre to be calculated. Having done this calculation the graded index fibre's other parameters such as propagation constant, V value and cut-off wavelength becomes much simpler. The equivalent step index fibre may be found either through computational analysis [2, 3] or by measurement [4].

The primary benefit of multimode graded index fibres over those containing a step index is a reduction in modal dispersion. Each mode of a step index fibre will have a different group velocity despite having the same wavelength, these differences limit the bandwidth of the fibre. The fundamental mode of a step index fibre will have the highest group velocity, higher order modes of the fibre will have lower group velocities and so arrive at the output end of the fibre with some delay. However, through control of a varying refractive index across the fibre core such as that seen in a graded index fibre the group velocity of the higher order modes can be increased compared to that of the fundamental. In the case of the fundamental the mode profile concentrates the power in the centre of the core, where the refractive index is highest. Higher order modes on the other hand will typically have a greater proportion of the modes power away from the central axis of the fibre, in this region of a graded index fibre the refractive index will be lower than at the centre. Meaning that the differences in group velocity of these higher order modes and the fundamental can, through careful design of the index profile, be minimised. It is worth noting at this point that there is no known profile that will cause all modes of the fibre to become completely equal.

1.3 Propagation Constant

The ray description of optics used to describe total internal reflection can only take us so far. In many optical fibres the core diameters are comparable to the wavelength of guided light. The wave nature of light must therefore be considered, in particular the effects due to diffraction. In an optical fibre of this type one would expect the tight confinement to produce a large divergence angle, but in an optical fibre the index step has a focusing effect exactly compensating for the divergence for certain field distributions. The certain field distributions for which this takes place are the modes of the fibre. These field distributions or modes are solutions of Maxwell's equations [5]. The geometrical parameters of the optical fibre along with the refractive indices of the core and cladding glasses provide the boundary conditions [1]. For a mode of an optical fibre the component of the wavevector k parallel the propagation axis is known as the propagation constant β. The propagation constant of a mode describes the evolution of the phase as it propagates, owing to the vector being parallel to the core-cladding boundary inside the fibre it is consistent across this interface. This consistency makes the propagation constant useful in describing modes of an optical fibre as the only the input and output of the fibre are non-parallel. For guidance by the core the allowed values of β are limited by the refractive indices of the core, n_{cl}, and cladding, n_{co}, providing the upper and lower bounds respectively show in equation

$$n_{cl}k_0 \leq \beta \leq n_{co}k_0 \tag{1.5}$$

where k_0 is the free space wavevector equal to $2\pi/\lambda$. The propagation constant on lower bound of β is the maximum value allowed to propagate through the cladding, leading to light launched into the core with a higher propagation constant than this being trapped. The guided mode with the highest propagation

constant is known as the fundamental mode of the fibre. It is also possible to define an effective refractive index for a given mode using the propagation constant

$$n_{eff} = \frac{\beta}{k_0} \tag{1.6}$$

The effective refractive index is also known as the modal index because of its dependence on the mode the light is propagating in, it is also dependant on the wavelength of the mode (through the free space wavevector k_0).

1.4 Origin of V parameter

In this section the difference between the core and cladding refractive indices in the optical fibre is small. This means that weakly guiding conditions cans be assumed, allowing the use of scalar wave analysis [6]. Only the transverse components of the fields need to be included in the solutions because fields propagating in the z-direction (along the axis of the fibre) are common to all solutions.

The field distributions are solutions of the scalar wave equation,

$$\nabla_t^2 \psi + (k_0^2 n^2 - \beta^2)\psi = 0 \tag{1.7}$$

where ψ is the transverse component of the field, ∇_t^2 is the transverse Laplacian operator, k_0 is the wave number and n is the refractive index of the medium and β is the propagation constant. For ease 1.7 is converted into the cylindrical polar coordinate system,

$$\frac{\partial^2\psi}{\partial r^2}+\frac{1}{r}\frac{\partial\psi}{\partial r}+\frac{1}{r^2}\frac{\partial^2\psi}{\partial\varphi^2}+(k_0^2n^2-\beta^2)\psi=0 \tag{1.8}$$

using $\psi(r,\varphi)=R(r)F(\varphi)$ equation 1.8 may be solved by separating variables.

$$\frac{d^2R}{dr^2}+\frac{1}{r}\frac{dR}{dr}+\left(k_0^2n^2-\beta^2-\frac{l^2}{r^2}\right)R=0 \tag{1.9}$$

$$\frac{d^2F}{d\varphi^2}+l^2F=0 \tag{1.10}$$

where *l* is an integer. The solution of equation 1.10 is simply,

$$F(\varphi)=\begin{cases}\sin(l\varphi)\\ \cos(l\varphi)\end{cases}. \tag{1.11}$$

Degeneracy of the modes allow either sine or cosine to be used in equation 1.1. When propagating in the core region of the fibre, $r<a$ where a is the core radius, the solution of equation 1.9 is found, by inspection, to be of the form of a Bessel function [7].

$$R(r<a)=J_l\left(U\frac{r}{a}\right) \tag{1.12}$$

where $U=a(k_0^2n_1^2-\beta^2)^{1/2}$, and n_1 is the core refractive index. In the cladding region where $r>a$ the solution has the form

$$R(r>a)=K_l\left(W\frac{r}{a}\right) \tag{1.13}$$

where $W=a(\beta^2-k_0^2n_1^2)^{1/2}$.

Continuity at the boundary between core and cladding means the field value, ψ, and the gradient of the field, $\partial\psi/\partial r$, at $r = a$ must be equal in core and cladding. This leads to a transcendental equation that can be solve numerically for β,

$$U\frac{J_{l+1}(U)}{J_l(U)} = -W\frac{K_{l+1}(W)}{K_l(W)} \tag{1.14}$$

where J_{l+1} equivalent to the negative of is J_l differentiated. It is also worth noting that a dimensionless parameter V can be introduced by observing that

$$V^2 = U^2 + W^2 = a^2(n_1^2 - n_2^2)k_0^2. \tag{1.15}$$

Alternatively

$$V = \frac{2\pi a}{\lambda}\sqrt{n_1^2 - n_2^2} \tag{1.16}$$

From the previous equations it can be seen that a mode ceases to exist when $W = 0$, no decay in the cladding. For the first higher order mode this occurs when $J_0(V) = 0$, at which point $V = 2.405$. It can then be said that a fibre is single mode if $V < 2.405$.

1.5 Group Index

A wave of monochromatic light has, as it propagates, points of constant phase, known as a wave front. The speed at which the points of constant phase travel is the phase velocity v_p, given by

$$v_p = \frac{\omega}{\beta} = \frac{c}{n_{eff}} \tag{1.17}$$

where ω is the angular frequency of the wave and c is the velocity of light in a vacuum. This equation also demonstrates that the effective refractive index is the ratio of the velocity of light in a medium to the velocity of light in a vacuum. Monochromatic light is in practice however impossible to perfectly produce. Instead light wave is made up from a number of different components of different frequencies. In the case where the group of propagating waves have similar frequencies they form a wave packet. The wave packet formed does not travel at the phase velocity of its individual components but rather at the group velocity v_g [8], given by

$$v_g = \frac{d\omega}{d\beta} \tag{1.18}$$

In optical fibres the group velocity is important because it is at this speed that the observable envelope of an optical pulse moves [9]. It is also interesting to note that from the equations we find that the group velocity equals the phase velocity only when the angular frequency is directly proportional to the propagation constant.

The relationship between the group index and group velocity is analogous to the relationship between the effective index and the phase velocity. By taking an adjusted version of equation 18

$$v_g = \frac{d\lambda}{d\beta}\frac{d\omega}{d\lambda} \tag{1.19}$$

and substituting in using $\beta = n_{eff}k_0$, $k_0 = 2\pi/\lambda$ and remembering that $\omega = 2\pi c/\lambda$ we obtain

$$v_g = \frac{d\left(\frac{n_{eff}\,2\pi}{\lambda}\right)}{d\lambda}\left(\frac{-\omega}{\lambda}\right) \tag{1.20}$$

$$= \frac{\omega}{2\pi\lambda}\left(\frac{n_{eff}}{\lambda^2} - \frac{1}{\lambda}\frac{dn_{eff}}{d\lambda}\right)^{-1} \tag{1.21}$$

$$= \frac{c}{\left(n_{eff} - \lambda\frac{dn_{eff}}{d\lambda}\right)} \tag{1.22}$$

Equation 1.22 is comparable to 1.17 and from it we can see that group index n_g is given by

$$n_g = n_{eff} - \lambda\frac{dn_{eff}}{d\lambda} \tag{1.23}$$

As with phase velocity, the ratio of the group velocity of a wave packet in a medium to the velocity in free space is given by the group index.

1.6 Coherence length

Coherence is a term that can be used when describing both temporal and spatial properties of a propagating wave. In this section the focus will be on temporal coherence. Temporal coherence is typically quantified in terms of coherence *length* or coherence *time*. Coherence length is used instead of coherence time because the optical time delays involved in experiments are measured as differing optical path lengths through the use of an interferometer.

Finding an expression for the coherence length of a laser can be done by thinking about the wavelength range. Combining the wave with a copy of itself, each travelling along different arms of the interferometer, would result in a maxima where optical path lengths are equal. However the spectral width of the wave means that as you move away from this point the maxima of one wavelength will start to overlap with the minima of another. Here the interference fringe packet will disappear. For this to occur we can say that the optical path difference (OPD)

$$OPD = m\lambda_1 = \left(m + \frac{1}{2}\right)\lambda_2 \tag{1.17}$$

with λ_1 and λ_2 representing the bounds of the pulses spectral width and m being the number of wavelengths. Rearranging gives

$$m = \frac{OPD}{\lambda_1} = \frac{OPD}{\lambda_2} - \frac{1}{2} \tag{1.18}$$

$$OPD = \frac{\lambda_1\lambda_2}{2(\lambda_1 - \lambda_2)} \approx \frac{\lambda^2}{2\Delta\lambda} \tag{1.19}$$

where $\Delta\lambda = \lambda_1 - \lambda_2$ and $\lambda_1\lambda_2 \approx \lambda^2$ where λ is the central wavelength. This value for the optical path difference is from the centre of the interference fringe packet to one edge. The total width is therefore double, this is the coherence length l_c

$$l_c = \frac{\lambda^2}{\Delta\lambda} \tag{1.20}$$

which, so long as the wavelength interval is small, may be defined in terms of frequency as

$$l_c = \frac{c}{\Delta\nu} \tag{1.21}$$

However, when calculating for a pulse the time width of the pulse must also be considered. If the time width of the pulse is $\Delta\tau$ then the coherence length may be simply calculated by

$$l_c = \Delta\tau \times c \tag{1.229}$$

Using the time-bandwidth product (tbp) for a given pulse shape, e.g. Gaussian, the coherence length can be found in terms of wavelength

$$tbp = \Delta\nu\ \Delta\tau = \frac{2\ ln2}{\pi} \tag{1.30}$$

Using the same substitution as in 1.21

$$(\Delta\tau \times c)\frac{\Delta\lambda}{\lambda^2} = \frac{2\ ln2}{\pi} \tag{1.23}$$

and we can find the coherence length using 1.229

$$l_c = \frac{2\ ln2}{\pi}\frac{\lambda^2}{\Delta\lambda} \tag{1.24}$$

Perhaps as expected the coherence length for a pulse is similar to that of a continuous wave but with a factor to account for a pulse shape which shortens the total coherence length.

1.7 Measuring group index

The group index of a core in an optical fibre is affected by a number of parameter, as already seen, including wavelength, core diameter and numerical aperture. If all of the required values are known precisely the group index may be calculated, however in reality the fabrication of the optical fibre will lead to some uncertainty in these values (specifically core radius and numerical aperture) and it becomes necessary to experimentally measure the group index of nominally identical cores to distinguish any differences. Fundamentally this involves measuring the transit time of light of a given wavelength through a known length of fibre. This can be done using an interferometer, in this case a Mach-Zehnder interferometer.

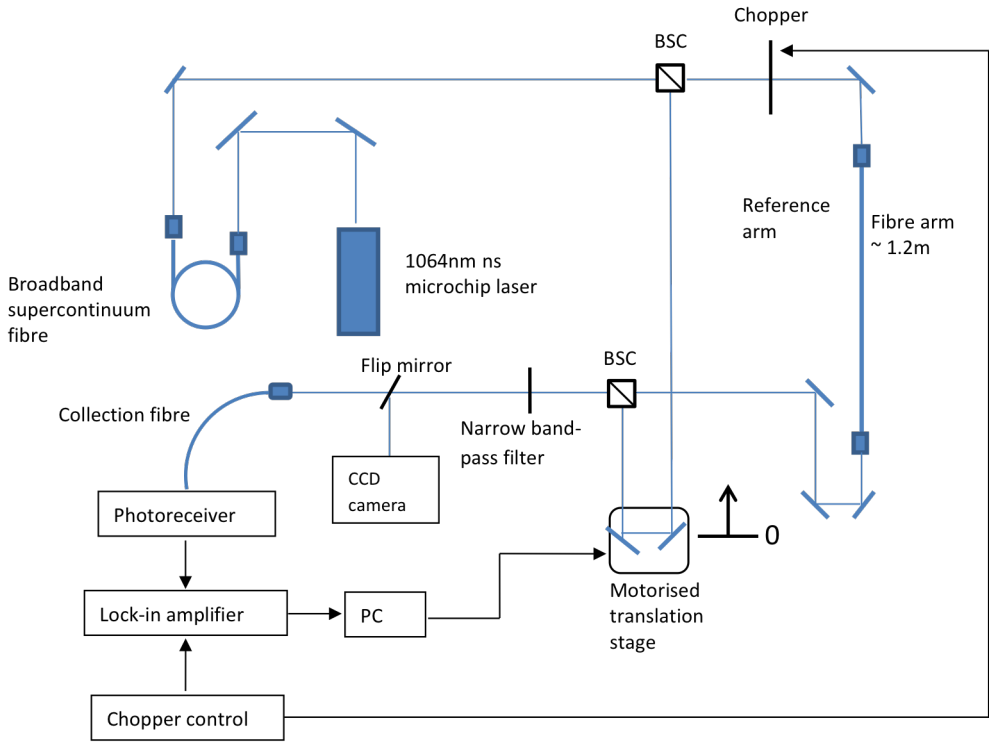

Figure 1.3: The experimental set-up used to measure interference fringe positions.

The experimental set-up is shown in figure 1.3. A nanosecond microchip laser at 1064 nm is the light source used. To generate the range of wavelengths required for the measurement the 1064 nm laser is coupled into a supercontinuum fibre to generate a white light spectrum. The white light passes through a beam splitter which creates the two necessary arms of the interferometer. One optical path is coupled into and through the fibre of interest and brought back to the second beam splitter cube. At the second beam splitter cube the fibre arm is recombined with the reference arm. The reference arm of the interferometer contains a motorised translation stage which is able to alter the geometrical path length of this second arm. The translation stage is controlled by a PC through a LabVIEW program. Once the beams have been recombined at the second beam splitter cube an interference filter is used to select the desired wavelength. A flip mirror can then be used to intercept the co-linear beams and redirect them towards a CCD camera to check the beam overlap and the assist with coupling into the chosen core of the optical fibre. Flattening the flip mirror allows the two beams to pass into the collection fibre and, via a photoreceiver and lock-in amplifier, the PC

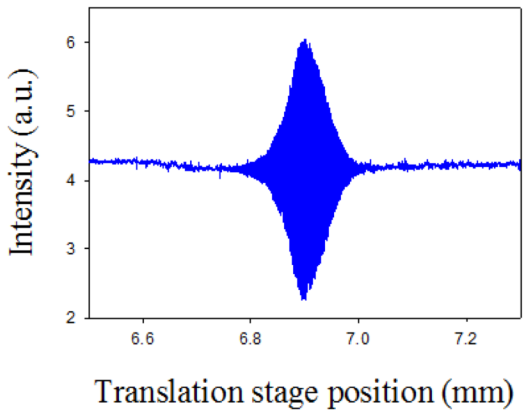

Figure 1.4: An example of an interference fringe obtained using the set-up in figure 1.3.

and LabVIEW program. The program then uses the translation stage position and light intensity to plot an interferogram. When the two arms of the interferometer are of equal optical path length an interference fringe is visible on the trace, an example of which is shown in figure 1.4.

To calculate the group index the difference of two fringe positions corresponding to two differing fibre lengths is required,

$$n_g = \frac{\Delta x}{\Delta L} + 1 \tag{1.33}$$

where x is the fringe position and L is the fibre length.

In the case of a multicore fibre where small variations in group index between cores is important particular attention must be paid when changing coupling from one core to another. This is done by only moving the ends of the fibre, rather than the lenses used to couple into it. Doing this ensures the interferometer outside of the fibre remains identical for each cores measurement. The flip mirror and CCD camera are valuable tools for identifying and coupling into successive cores as well as aligning the output with the reference arm.

1.8 Fibre Tapers

Creating a fibre taper is done by carefully heating and stretching a section of the fibre. Heating the fibre softens the glass and allows stretching to thin the fibre in the heated region. The core within the fibre reduces by the same factor as the total fibre diameter. The thinning region can be as little as a few millimetres or up to several centimetres in length. The point at which the fibre is at its thinnest is known as the fibre waist. If this transition from untapered fibre to the waist region is sufficiently gradual there will be little light loss from the fundamental mode of the fibre, in this the case the taper is adiabatic [10, 11]. An example of

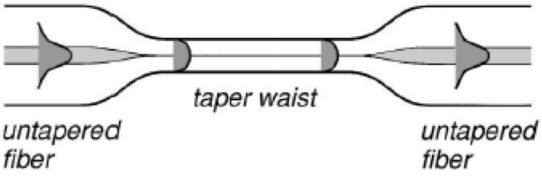

Figure 1.5: An example of a fibre tapered to a thin waist region and back to an untapered fibre [13].

a fibre tapered to a thin waist region and back to an untapered fibre is shown in figure 1.5. If the upward-taper region is also an adiabatic transition the whole device will exhibit low loss [12].

Fibre tapers are used in a range of applications. Mode matching tapers are used to alter the mode size within the optical fibre to improve coupling between two waveguides. Fibre tapers are also used as mode filters. As the diameter of the core drops through the taper this causes the V value of the core to drop along with it. In this way the V value of the core can be brought from a multimode regime to below 2.405. Here only light in the fundamental mode remains in the core of the fibre. The change in fibre properties can also be exploited to allow supercontinuum generation in tapered fibres [13]. The waist region may also be made narrow to the point that light is predominately guided by the air-glass

interface (not the core of the fibre) before an upward-taper returns light to the core of the fibre.

1.9 Fibre Losses

There are a number of mechanisms that can cause loss in an optical fibre. Some are intrinsic to the material such as infrared (IR) absorption and Rayleigh scattering. The inherent losses in silica are shown in figure 1.6. At short wavelengths density fluctuations in the glass cause Rayleigh scattering and at longer wavelengths IR absorption dominates owing to vibrational resonances of silica dioxide (SiO_2). Loss in a fibre can also be due to scattering and absorption by impurities such as hydroxyl ions (OH^-). This particular impurity would show up in figure 1.6 as a peak around 1.38μm.

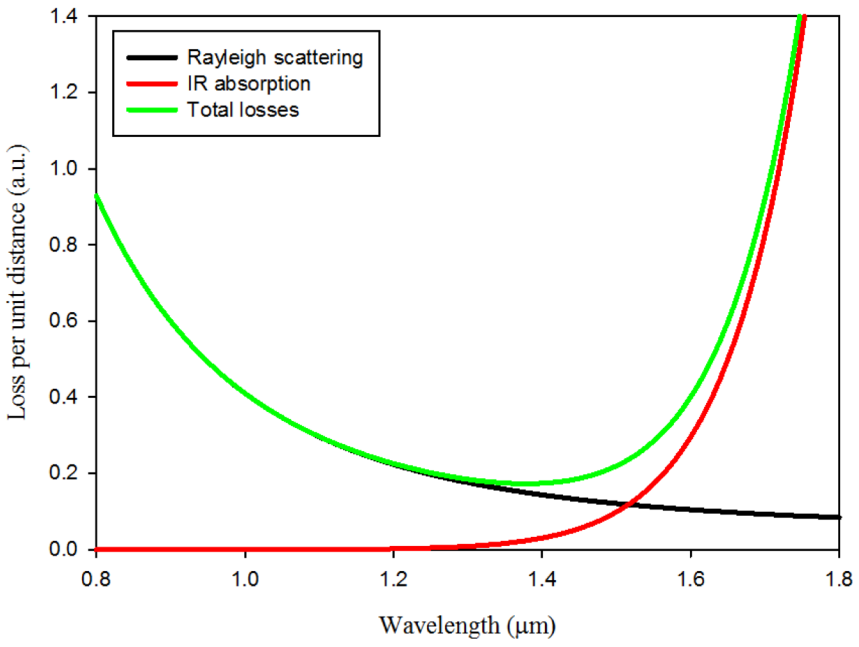

Figure 1.6: The intrinsic losses of silica. IR adsorption dominates at longer wavelengths and at shorter wavelength Rayleigh scattering is the main loss mechanism.

Loss in a fibre can also occur because of the design of the fibre. Confinement loss arises from insufficient confinement of light in the core due to the finite nature of the cladding. Light is insufficiently confined to the core when a significant part of the fibre mode extends past the cladding and is then lost.

The flexibility of an optical fibre also introduces another loss mechanism know as bend loss. A fibre will have a critical bend radius and bending it beyond this will introduce bend loss. For the mode to maintain a wavefront perpendicular to the direction of propagation at a bend in the fibre the part of the mode propagating on the outside of the bend must travel faster the light propagating in the centre. When the light on the outside of the bend is required to travel faster than the speed of light in that material to maintain a perpendicular wavefront it is lost through radiation as it would be impossible for it to do so [14]. It is this bend radius which is known as the critical radius.

1.10 Multicore fibres

Multicore optical fibres, as the name suggests, are optical fibres which contain more than one guiding core. The number of cores can range from only a few up to thousands. The family of multicore fibres can be further divided into holey multicore fibres and solid multicore fibres. Holey fibres contain a photonic crystal structure of silica and air with solid silica cores acting as defects within the structure and guiding light [15], figure 1.7(a). Solid multicore fibres use doped glass to guide light in their multiple cores. Multicore fibres can be further categorised into those with homogenous and heterogeneous cores. In fibres with homogenous cores the core spacing, known as the pitch Λ, becomes important when considering cross-talk. Increasing the separation between cores increases the coupling length. Fibres containing cores of differing sizes may be more closely spaced as the maximum power transfer between two cores decreases as the core diameters become more dissimilar [16, 17].

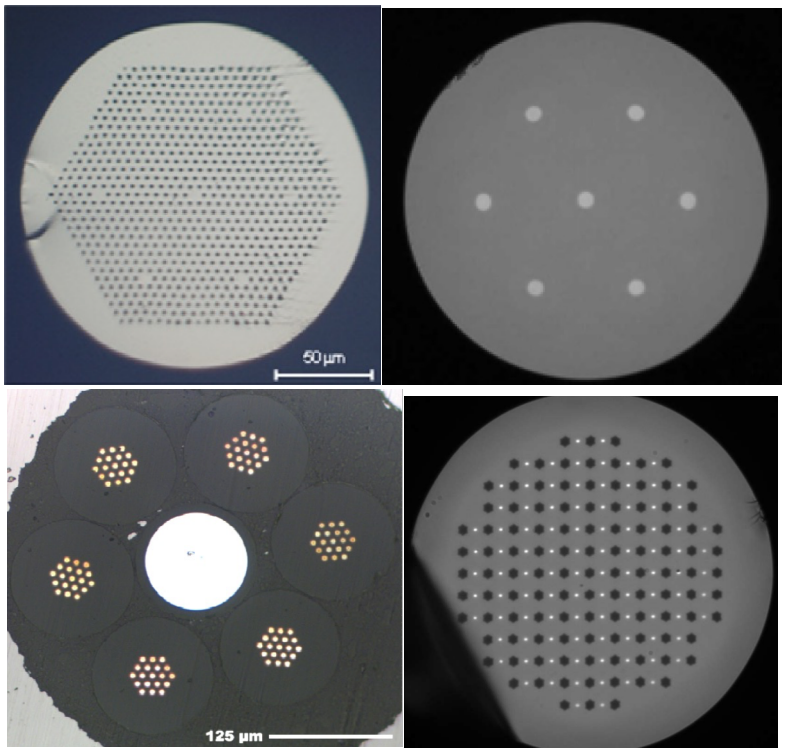

Figure 1.7: a) Seven core photonic crystal fibre [15]. b) Seven core fibre [16]. c) Endoscope fibre with six 19 core cells for light collection surrounding a delivery core [19]. d) Highly birefringent multicore fibre [20].

Motivation behind developing multicore fibres stems from an eclectic range of disciplines. From increasing transmission capacity in telecommunications fibres through spacial division multiplexing [18] to increased pixels for endoscopy. Here we are most interested in multicore fibres for endoscopy where information must be collected from the distal end of an optical fibre. Some fibres used multiple core to improve collection efficiency as in image (c) of figure 1.7 [19]. Others are able to collect information on polarisation using highly birefringent multicore fibre [20], figure 1.7(d). More typically however the number of cores is the driving factor and fibre bundles containing many thousands of cores are used for imaging the area of interest.

1.11 Fabrication

Both multicore fibre and conventional single core optical fibre can be made using the *stack and draw* technique. This entails creating a macroscopic version of the fibre design before it is then drawn down to the required microscopic size.

The *stack and draw* technique uses a furnace to soften the glass. The glass is fed into the top of the furnace and heated to approximately 2000˚C for silica glass (soft glasses become malleable at lower temperatures, a few hundred to a thousand degrees Celsius). The glass, once heated is pulled from the furnace at a greater rate than it is fed in. Through conservation of volume the drawn glass will have a smaller diameter. Knowing the outer diameter of the input glass allows good control of the drawn outer diameter through the relative feed and draw rates.

The first stage in fabricating a multicore fibre is drawing the doped rods which will create the individual cores within the fibre. In some fibre designs it is necessary to jacket these drawn doped rods with a silica tube, when drawn again a vacuum is applied to remove air from between the rod and jacket.

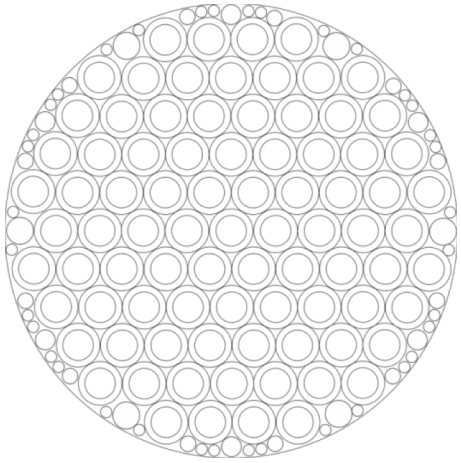

Figure 1.8: An example stack design for a multicore optical fibre. Double ringed circles representing the doped rods stacked within the design. Silica packing rods shown around the edges as single lined circles.

The rods are then stacked in a hexagonal lattice arrangement of the desired size. Once the stack is complete it is placed within a silica jacket tube. To reduce the empty space between the hexagonal lattice and the circular jacketing tube the corners of the lattice are removed and small silica packing rods are positioned to fill the resulting gaps, as seen in figure 1.8. The stack along with packing rods and jacket are drawn down under the application of vacuum to canes. This reduces the outer diameter from around 20 *mm* to between 2 *mm* and 5 *mm*. The final stage involves drawing the canes to fibre. The same process as in previous steps is used to reduce the outer diameter down to between ~100 μm and 1 *mm*. In this final stage a coating is added to the outside of the fibre to prevent scratches, making the fibre more durable. A schematic of the fibre and cane drawing process is seen in figure 1.9.

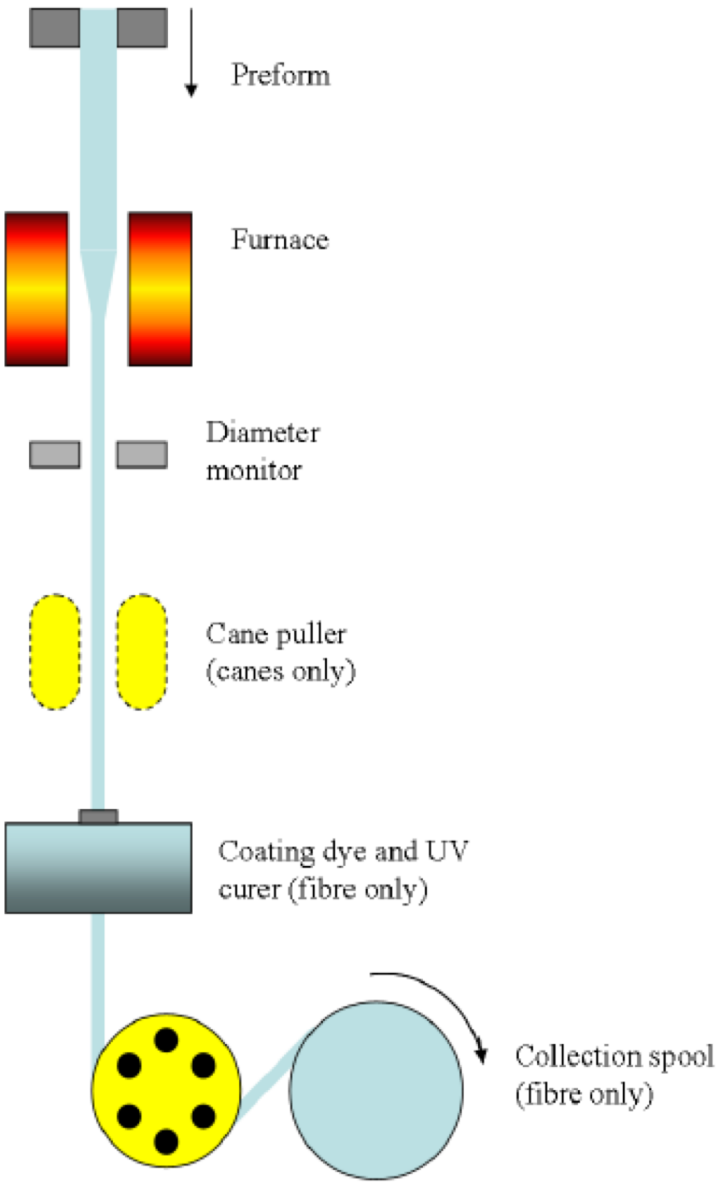

Figure 1.9: A schematic of the fibre and cane drawing process.

Chapter 2

Nonlinear endoscopy

2.1 Overview

Nonlinear optical imaging is now an essential tool for gaining high resolution images of cell processes and physiology. For this reason nonlinear imaging has become established in a wide range of biological and medical applications, in particular those involving cancer and neuroscience research [21-24]. At present these nonlinear imaging applications are mostly limited to the laboratory bench top, requiring invasive surgery and removal of tissue to perform the necessary imaging using nonlinear microscopy. Currently, *in vivo* imaging is predominantly limited to endoscopes offering images via linear optical scattering.

Combining the *in vivo* and minimally invasive capabilities of endoscopy and the enhanced imaging information available through nonlinear microscopy would result in nonlinear endoscopy. Allowing cellular imaging within tissue or organs previously unavailable to traditional nonlinear microscopy without invasive surgery. Without the need for surgery it also becomes possible to view biological processes *in vivo*.

The development of an endoscope capable of the same nonlinear imaging used in microscopy first requires an understanding of the nonlinear imaging processes in microscopy.

2.2 Introduction to nonlinear microscopy

Microscopy can be split into linear and nonlinear imaging techniques. Linear optical microscopy relies on a light-matter interaction which is proportional to the incident light intensity, a single photon process. Nonlinear microscopy is fundamentally different in that the light-matter interaction is a multi-photon process, this gives unique imaging properties.

Biological imaging uses several key nonlinear effects, including higher harmonic generation, multi-photon absorption and coherent anti-Stokes Raman scattering (CARS). The most popular method to generate image contrast amongst these techniques is two-photon absorption excited fluorescence. Compared to a single-photon interaction the excitation cross-section for a two-photon interaction is typically 40 orders of magnitude smaller [25, 26]. This is because the two-photons required for the interaction must excite the molecule simultaneously. For this a femtosecond pulsed laser in the near infrared is used, this localises the excitation in time as well as space.

Ultrashort pulses are also able to produce second or third harmonic responses in their interaction with biological samples or molecules, this generates higher harmonics of the probing laser frequency [27-29]. The production of a photon of exactly half the excitation wavelength requires two photons of that wavelength to interact simultaneously with the structure of interest [30]. This differs from two or multi-photon absorption because higher harmonic generation is a coherent process. Meaning that the isotropic radiation produced in multi-photon absorption is no longer seen and a predominantly forward-directed and highly polarised emission is seen. This property of harmonic generation removes the need for additional labelling when determining the orientation of structures and organisational degree of proteins.

CARS, another nonlinear process used in biological imaging, is able to give chemical specific information and is sensitive to molecular vibration states [31]. Molecular signatures can be found in the particular vibration states, the individual characteristics of the molecule. These signatures provide a fingerprint of the

molecule allowing the identification of the biochemical components within a tissue sample. This is inherently different from the contrast based imaging systems mentioned above. CARS has been particularly useful in the mapping of lipid compartments, protein clusters and water distributions in tissue.

The imaging systems talked about previously are crucial methods in providing non-invasive and high resolution images of three dimensional structures within tissue. They can be of even greater use in conjunction with one another. Used together second harmonic generation (SHG) and two-photon excited fluorescence (TPEF) have brought new insights and understanding to cancer research [32-35]. In this case complimentary information is provided by the intrinsic fluorophores within the sample (TFEF) and the extracellular environment (SHG). It is then clear that nonlinear imaging presents an attractive alternative to the use of stains and dyes necessary in histopathology to identify the structures and chemistry present within a biopsy specimen.

2.3 Obstacles to nonlinear endomicroscopy

The ability to performing *in vivo* nonlinear microscopy has the obvious advantage of no longer requiring a sample of tissue to be removed surgically. This allows a larger area to be examined with a minimally invasive procedure. Moving the techniques and bulky equipment used in nonlinear microscopy from the laboratory bench to an *in vivo* system naturally has a number of challenges associated with it. Rapid progress seen in optical fibres, micro-optics and micro-mechanics have given nonlinear endomicroscopy a promising start however as a discipline it is still at an early stage in its development. Some of the key obstacles facing endomicroscopy are discussed below.

The nonlinear modalities introduced previously (higher harmonic generation, CARS and multi-photon excitation) are intrinsically different mechanisms of imaging within tissue samples. The difference in the imaging mechanisms means that a diverse range of information that can be gathered when all methods are

available. In conventional microscopy under illumination of ultrashort pulses these effects are usually simultaneous, however since the first demonstration of a fibre-optic based nonlinear microscope [36] the chief nonlinear imaging mechanism has been TPEF [37-41]. Fibre based SHG microscopy is hindered by polarisation anisotropy inherent in the process and by the generated emission wavelength often lying outside the usual guidance window of the delivery fibre. To fully exploit the capabilities of nonlinear endomicroscopy the full range of imaging techniques must be realised.

A second concern for *in vivo* imaging techniques is acquiring the necessary light levels for nonlinear interaction after delivery and the returned signal after collection. This is of particular concern for single mode fibres (SMF). Temporal and spectral broadening seen in ultrashort pulses (~80-200fs) through SMF due to group velocity dispersion, self-phase modulation and cross-phase modulation [42], cause significant reductions in the penetration depth and nonlinear excitation efficiency. In addition to this, the low numerical aperture and small core typically associated with SMF causes the fibre to be susceptible to aberrations in the system. This in turn restricts the size of the collection area from which the emitted nonlinear signal may be gathered. Alternatively a fibre with larger NA and core size may be used, such as a multimode fibre (MMF), to increase the strength of the collection signal. This is not the answer however; a near diffraction-limited focal spot is needed for an efficient and high resolution nonlinear response in the sample. The multiple modes within the delivery signal of the MMF mean this is not possible. The use of multicore fibres allows the resolution of a couple of these issues. The high intensity delivery signal may be split over the multiple cores of the fibre, reducing the nonlinear response in each core. Each core may also be single mode, removing the focussing difficulties arising from multiple modes within each core. Despite the low NA of the individual cores the number of cores across the fibre end are able to create a much larger collection area than that of a single SMF.

In order for a two-dimensional image to be formed a scanning mechanism must be combined with the remote delivery of light by an optical fibre. In conventional endoscopy there are two common scanning mechanisms, proximal and distal scanning. In proximal scanning typically a pair of mirrors is used to raster scan across up to 100 000 cores in the imaging fibre bundle [43, 44]. The diameter of the complete fibre is less than 3 mm and has an NA ~ 0.3. Each core within the fibre is used for delivery of the laser source individually but all cores are used for collection of the signal. A composite image is formed from the information gathered using each of the cores. For distal scanning either the fibre tip or the light coupled from the fibre must be moved to effectively scan the area of interest [45, 46]. A piezoelectric bending element or an electromagnetic actuator can be used near the mechanical resonance of the fibre tip to create various 2D scanning patterns. These scanning mechanisms are too slow and bulky to be applicable for nonlinear optical endoscopy. For successful application the mechanism must be less than ~3 mm and scan rapidly enough to study fast processes and avoid photo-bleaching.

A conventional endoscope's mechanical flexibility and compact arrangement must be preserved. The ability of a nonlinear endoscope to work as a solo piece of equipment or be incorporated into the working channels of an existing clinical endoscope and be inserted in the body is its main advantage over conventional optical microscopy.

Nonlinear endomicroscopy review

Since the introduction of nonlinear optical imaging techniques the additional information provided by them has been exploited by microscopy to provide medical diagnosis on the laboratory bench. The ultimate goal of nonlinear imaging has naturally then been to provide *in vivo* medical diagnoses. Fibre optics are the foremost system for developing such techniques within humans. The minimally invasive manner with which light pulses may be delivered and collected is the primary reason for this. Among the many advantages that fibre-optics offer to imaging systems are mechanical flexibility and improved optical sectioning. Linear fibre-based imaging systems already able to perform bed-side minimally invasive clinical diagnostic and surgical procedures in living subjects [47, 48].

An in-depth study of nonlinear optical endoscopy requires a thorough understanding of the nonlinear optical processes that may occur within the imaging techniques.

2.4 Nonlinear imaging processes

Since the first demonstration of SHG with a pulsed ruby laser in 1961 [30] the field of nonlinear optics has been developing at a prolific speed. Over the previous couple of decades the advancement of imaging techniques based on nonlinear optical processes has been boosted by the swift progress in laser scanning microscopy, mode-locked femtosecond lasers and the creation of improved fluorescence markers. Nonlinear optical microscopy has become a handy tool in the biological sciences using the high spatial resolution available from the higher-order dependence on the excitation intensity necessary for the interaction.

These optical effects can be used as imaging contrast mechanisms when the sample interacts with light of a high enough intensity to produce a nonlinear

response to the applied field strength. In these light-matter interactions, the induced polarisation of the material subjected to the electric field may be expressed as [30]:

$$P = \chi^{(1)}E + \chi^{(2)}E^2 + \chi^{(3)}E^3 + \cdots \quad (2.1)$$

where $\chi^{(i)}$ is the i^{th} order nonlinear susceptibility tensor. Materials containing delocalised electrons will typically give large nonlinear optical responses. The linear susceptibility $\chi^{(1)}$ contributes to the absorption and reflection of light in materials. Second harmonic generation (SHG) results from $\chi^{(2)}$ while $\chi^{(3)}$ corresponds to third-order processes such as two-photon absorption, third harmonic generation (THG) and coherent anti-Stokes Raman scattering (CARS). Mixing these nonlinear imaging techniques unsurprisingly extends the useful range of nonlinear optical microscopy. Though this thesis is principally motivated by two-photon excited fluorescence (TPEF) the nonlinear optical effects mentioned above will be reviewed.

2.5 Multi-photon fluorescence microscopy

In 1931 Göppert-Mayer first predicted multi-photon excitation. He was able to show theoretically that it is possible for multiple photons to be simultaneously absorbed by a material, achieving an excited state that corresponded to the sum of the energy of the individual incident photons, figure 2.1. Two-photon absorption was first demonstrated experimentally in CaF_2:Eu^{3+}, this was shortly after the previously mentioned first demonstration of SHG, and also relied on a pulsed ruby lasers [49]. A few years later in 1964 three-photon excited fluorescence was achieved for the first time using naphthalene crystals [50], the ringed hydrocarbon structure providing readily available delocalised electrons that aid the higher-order nonlinear process. Multi-photon excitation was subsequently then applied to the field of molecular spectroscopy. The invention of two-photon laser scanning microscopy by Denk et al. in 1990 [51] began the

move into biological applications for multiphoton absorption. In 1996 three-photon fluorescence microscopy was also described and its particular ability to use the inherent UV fluorescence of molecules present within cellular processes was shown [26, 52-54].

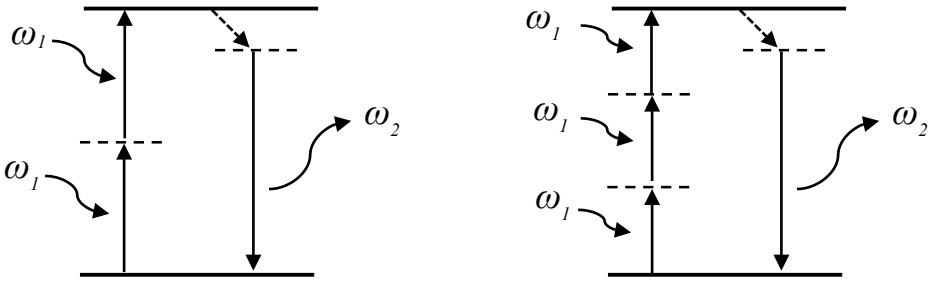

Figure 2.1: Left - 2PEF. Right - 3PEF.

The efficiency of multi-photon absorption depends on the multi-photon absorption cross section of the molecule and on two or more photons interacting with a molecule simultaneously. Therefore, the use of ultrashort-pulsed lasers will give the maximum fluorescence output available for image formation. For an *n*-photon process with the excitation laser pulses having width τ at a rate of *f*, the fluorescence is improved by a factor of $1/(\tau f)^{n-1}$ when compared to continuous wave illumination [21]. The rapid drop off of fluorescence strength away from the focal plane allows inherent 3D resolution without the need for additional confocal detection optics, as used in confocal microscopy to eliminate out of focus light.

In multi-photon fluorescence microscopy, only ballistic (nonscattered) photons efficiently contribute to the fluorescence generation in the focal zone. The two-photon excited fluorescence signal at imaging depth *z* is proportional to e^{-2z/l_s}, where l_s is the mean free path, describing the scattering strength of tissue. Typically, near infrared light is used in multi-photon fluorescence microscopy due to the lower scattering strength of the majority of biological tissue at these wavelengths. Therefore a comparatively deep penetration depth is able to be

achieved compared to confocal microscopy [55-57]. Additionally, multi-photon fluorescence microscopy uses wide-field detection. Meaning both nonscattered photons from the focal zone and numerously scattered fluoresced photons are collected and contribute to the image. Thus, the efficient excitation and collection available with multi-photon florescence microscopy make it an ideal tool to image deep within biological tissue.

The combination of different fluorescence regimes allows multicolour imaging. Multicolour imaging occurs when different fluorophores are simultaneously excited using a single excitation wavelength. Fluorophores may then use different order processes to emit separate wavelengths. Each of which is collected producing separate information on the various fluorophores. Multiphoton fluorescence microscopy is therefore able to offer valuable flexibility when studying a sample that could respond to two-photon, three-photon or a combination of the fluorescence modalities.

2.6 Harmonic generation microscopy

Nonlinear optical microscopy may be further extended by the use of harmonic generation (SHG and THG). In harmonic generation the energy of two or more incident photons is not absorbed but is scattered by the molecule via a process of harmonic up-conversion [58, 59]. SHG was the first demonstration of a nonlinear optical process [30]. Shortly after the first demonstration of SHG it was used for characterisation in spectroscopy and for frequency doubling in lasers. The first time SHG was used in conjunction with optical microscopy was in visualising the crystal structure of ZnSe [60]. However, the first demonstrated use of SHG for a biological imaging experiment was 12 years later in 1986 [61]. Here SHG was used to examine the orientation of collagen fibres in rat tail tendon. However only in the last decade has harmonic generation microscopy been fully established in imaging the tertiary structure of proteins inside biological tissue due to the advance in commercially available femtosecond lasers [62-65]. Only

slightly behind the advances in SHG imaging THG microscopy has also been emerging as a powerful tool [66-69].

Since harmonic generation microscopy is based on nonlinear optical processes, it retains the benefits of multi-photon excitation microscopy, such as the intrinsic 3D sectioning ability and a relatively greater depth penetration. The imaging mechanisms differ from those in multi-photon absorption. In harmonic generation there is no excited state, figure 2.2. Meaning there is no energy deposited into the tissue, this permits the noninvasive imaging of thermally delicate areas and making it desirable for certain clinical applications. Additionally, harmonic generation is a coherent processes. The phase of the produced harmonic closely resembles that of the fundamental excitation light. This leads the harmonic light to display a significant dependence on the spatial distributions of both the interacting molecule and the field of the fundamental light.

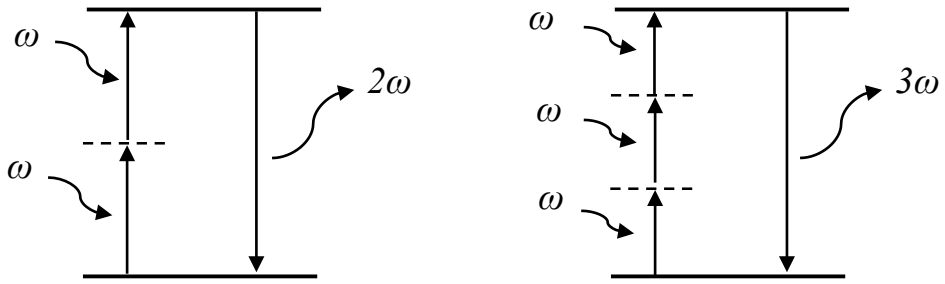

Figure 2.2: Left - SHG. Right - THG.

The coherent emission from harmonic generation allows information to be gathered on the molecular organisation and nonlinear susceptibilities within the sample (not available from fluorescence where phase is random), this is done by using the polarisation dependency of the generated harmonic light [70-73]. Polarisation is already present in conventional microscopy where it is used to examine the linear birefringence of samples. Using harmonic generation however the absolute orientation of molecules may be found by using random

combinations of the fundamental and harmonic polarisation states [29]. Another upshot of harmonic generation being a coherent process is that emission is broadcast in the forward direction. Therefore is becomes necessary for a transmission-collection geometry to be used in most cases. In disorganised tissue however, if the sizes of the scatters are approximately equal to the illumination wavelength, then that combined with the Gouy phase shift present due to the beam passing through the focus will cause a reduction on the forward emission profile [64, 70]. As a result, pronounced backward SHG is seen, allowing delivery and collection from the same point possible [33, 74].

Only materials comprising of either molecules or a unit cell lacking a centre symmetry at their heart (noncentrosysmmetric) will have a non-zero second-order susceptibility $\chi^{(2)}$, in centrosymmetric materials SHG is not possible. Contrastingly, THG may be applied to all materials due to the ever present nature of $\chi^{(3)}$. In the early days of SHG imaging stains such as styryl were used to dye collagen fibres and cell membranes to improve SHG efficiency [75-79]. More recent work has discovered that numerous structural protein assemblies give large SHG signals without the need for additional molecular labelling. SHG has been used to examine the effects of diseases in the skin, muscle, cornea, and brain pathology all through imaging of the extracellular matrix [34, 65, 80, 81]. SHG is also a vital tool in cancer detection. Studying the change in structure of collagen within tumors has shown that transformed cells display increased motility [34, 74, 82]. Through a combination of SHG and TPEF (imaging the protein structures and fluorophores respectively) the visualisation of cancer cell movement *in vivo* may be studied to understand the process by which cancer spreads from one organ to another [24, 74].

2.7 Coherent anti-Stokes Raman scattering microscopy

Coherent anti-Stokes Raman scattering (CARS) microscopy is another high-resolution imaging method which is able to produce 3D pictures without the need for additional chemical labels to be added the sample. As seen in figure 2.3,

CARS is a four-wave mixing process. A pump wave at frequency ω_p, a Stokes beam at frequency ω_s, and a probe beam at frequency ω_p' are mixed within a

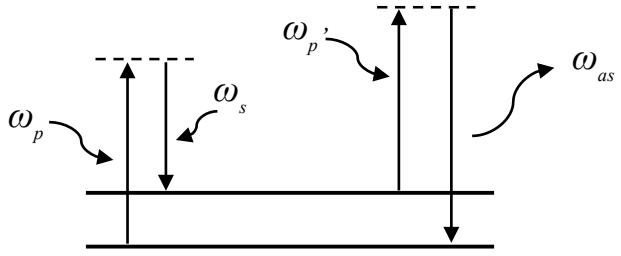

Figure 2.3: Energy levels used in CARS process. Dashed line – virtual energy level. Solid line – Actual energy level.

sample to result in an anti-Stokes signal at $\omega_{as} = \omega_p - \omega_s + \omega_p'$. CARS may be easily understood by considering the vibrational energy levels of the interacting molecule.

Starting with the molecule in the ground state the pump beam first excites the molecule to a virtual state. This virtual state allows for transitions between uncoupled real states but cannot itself be occupied. During this interaction if a Stokes beam is also present then the virtual state provides as an intermediate short-lived level giving access to an alternate vibrational state of the molecule. Through the combined action of the pump and Stokes beams an effective coupling between the two states of the molecule can be created. The two states simultaneously occupied by the molecule produces a coherent superposition of these states. Exciting the coherent superposition of the states with the probe beam this time promotes the system to another different virtual state. The virtual state, as before, may only be occupied instantaneously. The molecule then returns to a single (ground) state through the emission of a photon at a new frequency, the anti-Stokes frequency. During the CARS process no energy is deposited into the molecule, however a similar Raman process occurs alongside during which energy is deposited into the molecule.

In 1965 the first systematic study of CARS was completed [83]. Compared to the corresponding spontaneous Raman response CARS signals are orders of magnitude brighter, for this reason CARS spectroscopy is the most widely used nonlinear Raman technique. Similar to other nonlinear imaging processes the rapid progress made in the last decade [31] is primarily thanks to advancements in pulsed laser technology. The longer picosecond pulse lengths typically used in CARS, compared to those used in multi-photon and harmonic generation microscopy, support higher spectral resolution from a narrower bandwidth. This is particularly useful for probing a specific vibrational mode of a molecule.

The mechanics of CARS microscopy lead it to be particularly well suited for vibrational imaging of lipids, proteins and chromosomes in unstained cells. Its ability to pinpoint specific molecules make it ideal for recording molecules distribution and diffusion through biological matter. Recently CARS has demonstrated its chemical imaging possibilities [84] by differentiating between tissue structures based on the individual chemical compositions. Simultaneous vibrational and fluorescence imaging of samples has been demonstrated using CARS and multi-photon fluorescence [85]. The chemical specific information available through CARS imaging provides an excellent contrast to the predominately structural information obtainable by SHG and TPEF.

Chapter 3

Minimising group index variation

The work presented here describes a multicore fibre for nonlinear endoscopy where the constituent photons of an ultrashort pulse are propagated via multiple cores to reduce the nonlinear effects within the fibre. The variation in group index between cores of the fibre is minimized to allow the simultaneously launched sub-pulses to arrive at the distal end of the fibre synchronously. Minimization of group index variation between cores is achieved at a *V* parameter of 3 owing to a turning point in the relationship between the group index and *V* parameter. For synchronized arrival times single-mode propagation is important. By tapering a short length of the fiber at the launch end the *V* value is locally brought below 2.405 allowing a pure fundamental mode to be launched into each core

3.1 Introduction

As previously discussed endoscopy is used in a range of applications to remotely image samples where direct access is not possible. The combination of endoscopy and the nonlinear imaging techniques used in microscopy would provide novel information in formerly inaccessible regions of the body. The high peak powers required to generate these nonlinear responses from the *in vivo* sample have often been too high a hurdle. For example, a typical Ti:Sapphire laser producing ~100fs pulses of 20-30nJ, as often used in two photon microscopy, would be almost 4 times longer after 1m of propagation in typical SM optical fibre. The technique of splitting the power between multiple cores of a fibre stated earlier provides a method of navigating around this obstacle. When

the pulse energy is separated between the one hundred or so cores of the fabricated optical fibre this broadening becomes insignificant.

The short duration of the high powered pulses also requires that they are delivered to the sample almost simultaneously. Additionally, the phase of each pulse must be individually controlled using a Spacial Light Modulator (SLM). An SLM at the input of the fibre would allow control of the phase in each core. Through this, the scanning focal point is able to build a complete image of the sample. In this chapter we demonstrate how to design and implement a multicore fibre endoscope in which variations in group index between the cores are minimized, allowing for the physical and temporal delivery of short high powered pulses to the distal end of an optical fibre.

3.2 Design and Fabrication

Initially a multicore fibre preform was fabricated with nominally identical step-index cores and drew it to be single-mode at 800nm wavelength. However, measurements showed that there was significant variation in group index between the cores. These differences arise from core-to-core variations in diameter and numerical aperture. This is a result of the stack and draw technique

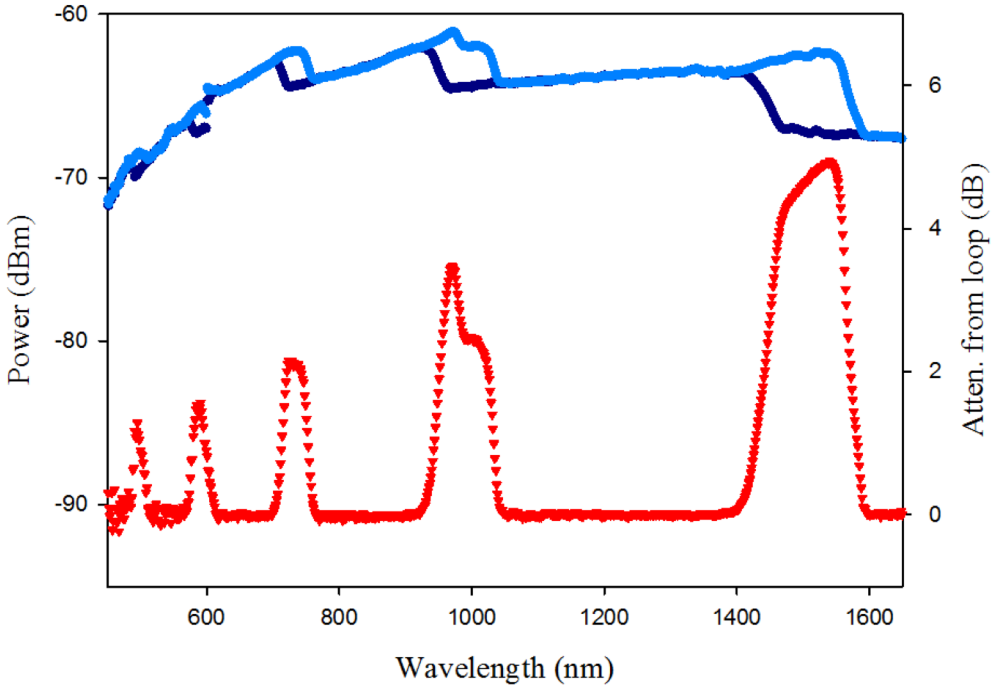

Figure 3.1: Blue lines – Power transmitted through a straight section of fibre (light blue) and the same section with a loop of diameter 2cm (dark blue). Red triangles – Attenuation due to the 2cm loop in the fibre. Showing wavelength of each subsequent mode cut-off until the fibre becomes single mode above ~ 1600nm.

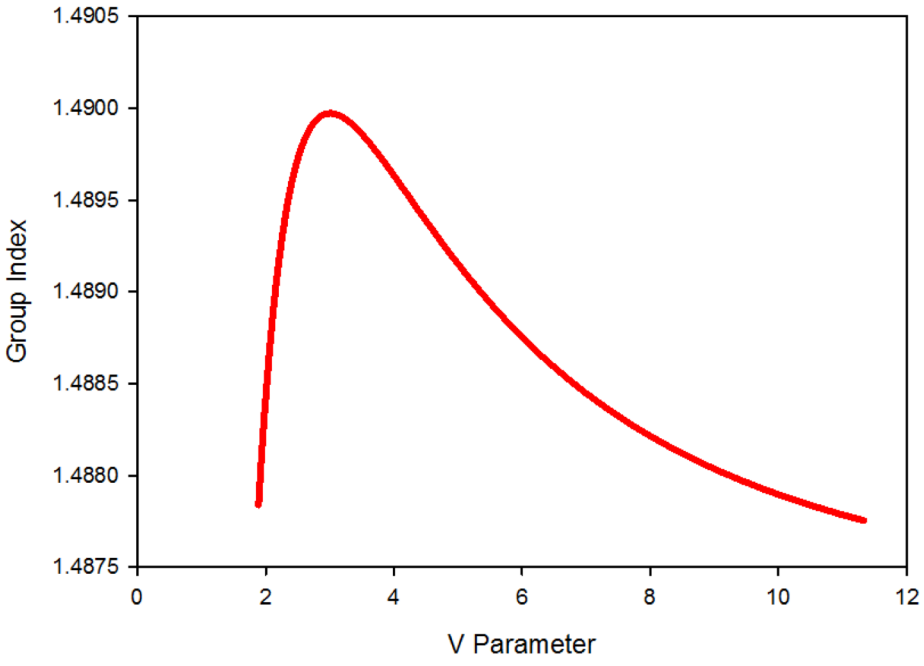

Figure 3.2: Numerical calculation of the group index at 800 nm for a single core of 1.36% index step. The turning point is seen near V=3.

used to fabricate the fibre and of changes in dopant concentration along the length of the single-core preform used to make the stack.

To address this, the dependence of the group index on fibre parameters was studied. Graded-index doped glass is used in the multiple cores of fibre. However, for the purposes of calculating group index it is easier to consider a step-index boundary. An effective step-index may be found for a graded-index profile through experimental measurement of the cut-off wavelength for modes within a fibre [8]. Figure 3.1 shows the transmitted power through an optical fibre with known core size for both a straight length of fibre and a section containing a loop of 2cm in diameter. As each mode approaches its cut-off wavelength it spreads out and becomes increasingly subject to bend loss. Conventionally, the wavelength at which the attenuation reaches 0.1dB above the long wavelength base line is classed as the cut-off wavelength [8]. The attenuation due to bend

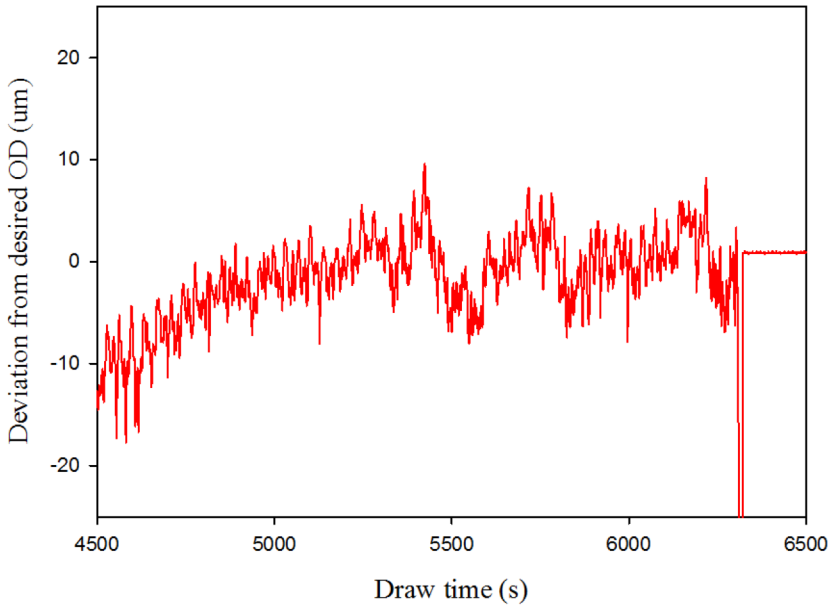

Figure 3.3: Diameter deviation from 1.7mm of germanium doped rods during draw phase of fabrication. Collection of rods only occurred with ±0.5% or ±8.5µm.

loss is seen in figure 3.1 as the red triangles. Using four different sizes of fibres an effective index step of 1.36% was measured.

As seen in figure 3.2 the effective index step is used to calculate the dependence of group index on the fibre V parameter, at a wavelength of 800 nm, as used for the fabricated fibres. The calculation took account of the material dispersion of the silica glass. The dependence of group index on core diameter is minimized near $V = 3$. This is a general result for a step index fibre, where the material dispersion is not too exotic, and is closely related to the $V = 3$ zero in the waveguide dispersion [86].

Using this information a 121 core preform was fabricated using the stack and draw technique. The desire for uniformity throughout the doped cores of the fibre meant that particular care was taken through the fabrication of the preform. The allowed tolerances at the draw stage being ± 0.5%. Figure 3.3 shows an example of an acceptable level of diameter deviation in a 1.7mm rod. Any rods drawn

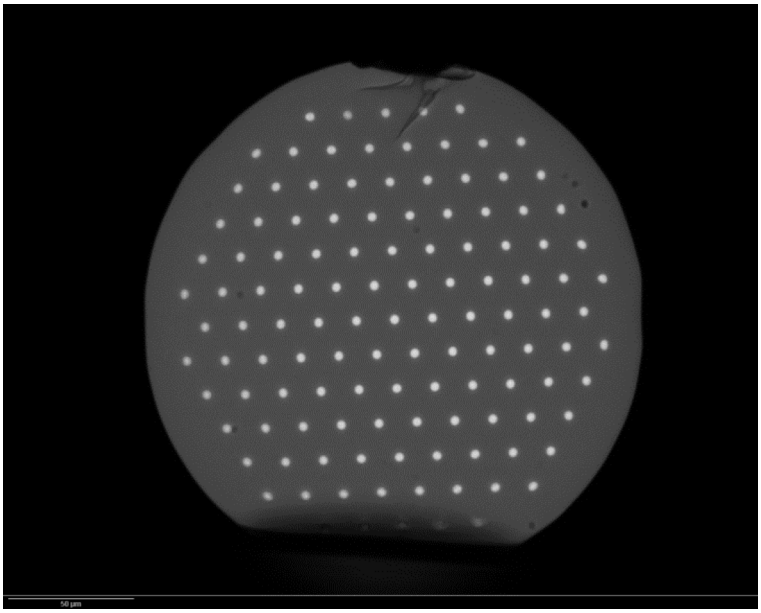

Figure 3.4: Optical microscope image of a 200μm diameter multicore fibre end face using bottom illumination.

with a diameter outside the desired range were discarded. From this 121 core preform a number of different multicore fibres were drawn to different outer diameters. The outer diameters of the multicore fibres directly related to the core size within. An example of one of the multicore fibres is shown in figure 3.4.

3.3 Experiment and results

The variation in group index amongst the various multicore fibres was measured using a low coherence scanning Mach-Zehnder interferometer utilizing a fibre-based optical supercontinuum with a 10 nm band-pass filter centred at 800 nm as a low-coherence light source (as discussed previously). The input and output ends of the sample fibre were translated with respect to the coupling lenses in order to study different cores while maintaining the path outside of the optical fibre constant.

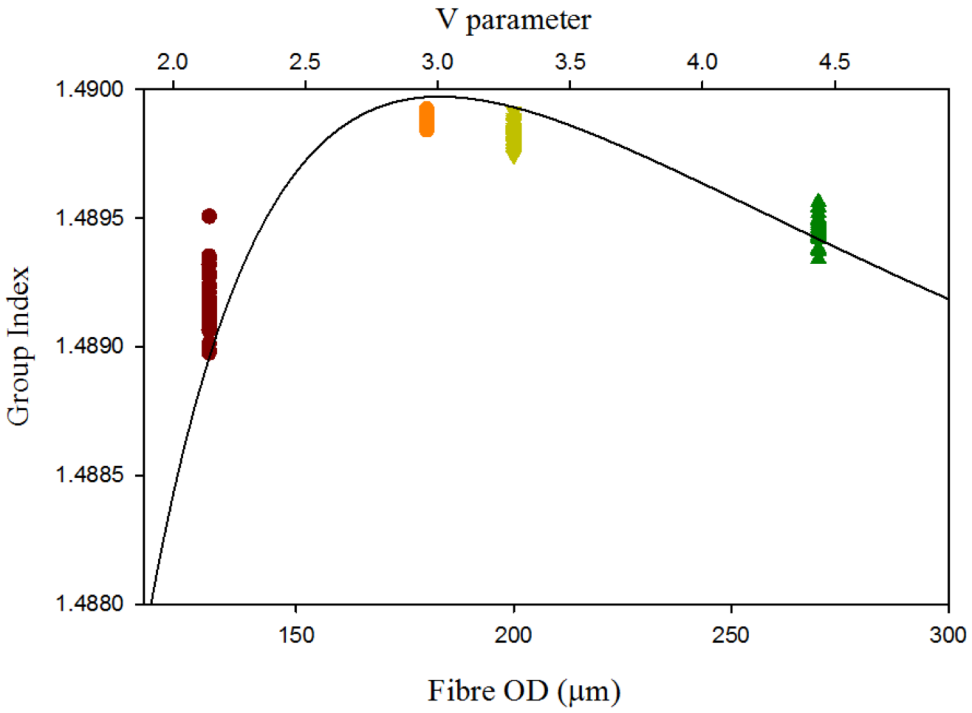

Figure 3.5: Line - calculated values of group index as from Figure 3.2. Points - measured group index of all 31 cores along the diagonals in 4 fibres, classed by fibre outer diameter and calculated *V* value.

Different core sizes were studied by selecting fibres of different outer diameters. For each fibre drawn the group indices of the 31 cores lying along the three diagonals in the array of cores were measured. This provided a representative sample of the variations in group index across each multi-core fibre, because the fibres were drawn from the same preform it also has the benefit of ensuring that the same cores were measured in each of the fibres studied.

Figure 3.5 shows the calculated variation of group index and the individual measured group indices of the 31 cores in each of four multicore fibres as a function of *V* and outer diameter (OD). The fibre with $V = 3$ (180 µm OD) shows the smallest spread of group indices across the 31 cores. The standard deviation of the group indices in the 180 µm this fibre is 2.2×10^{-5}, which is a variation of ~0.005%. In contrast, the standard deviation for the 130 µm OD fibre is approximately six times greater. Looking at figure 3.6 (which shows the standard deviation of the measured group indices of each fibre and the gradient of the

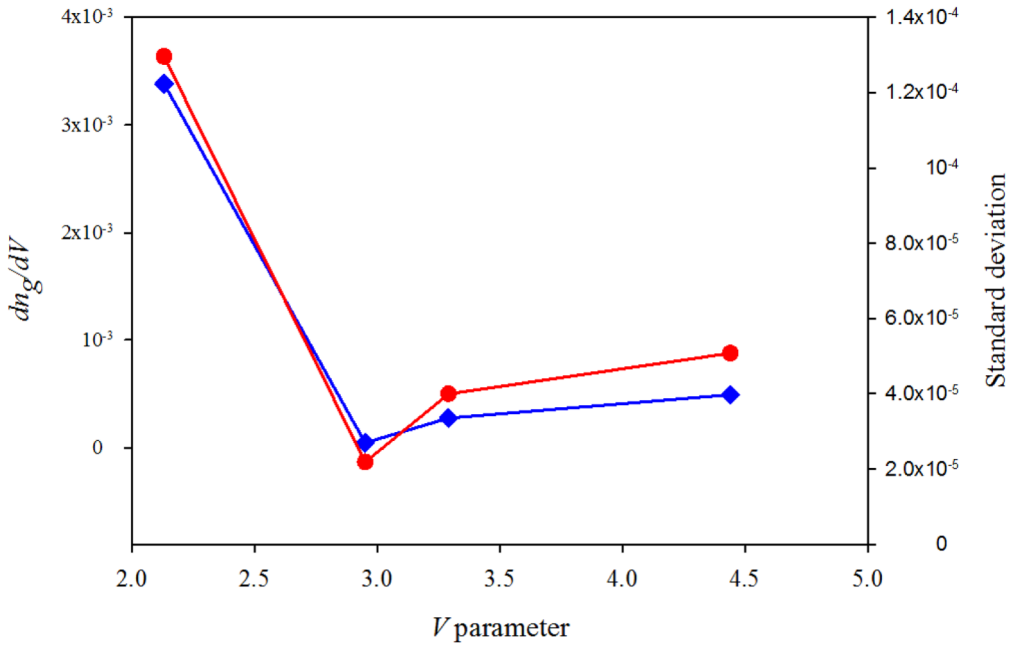

Figure 3.6: Blue (left axis) – Gradient of the group index simulation at each of the four fibre sizes measured. Red (right axis) – The standard deviation of the experimentally measured group indices for each of the four fibres.

calculated group index curve) the expected relationship between gradient and standard deviation is seen. The steeper the gradient the more sensitive the group index would be to small fluctuations and variations in core diameter. Conversely, at $V \approx 3$ where the gradient is approximately zero we see the smallest deviation in group indices.

From the standard deviation measured in the $V = 3$ fibre, it may be calculated that 100fs pulses with a central wavelength of 800nm simultaneously launched into the separate cores would still coherently recombine at the distal end after 2m of propagation.

The residual variation in group index seen in the $V = 3$ fibre is due to variations in the doping profile of the germanium doped canes from which the multicore

preform was made. Using the doping profile data supplied with the germanium-doped preforms figure 3.7, the radius of the doped region in these preforms varied

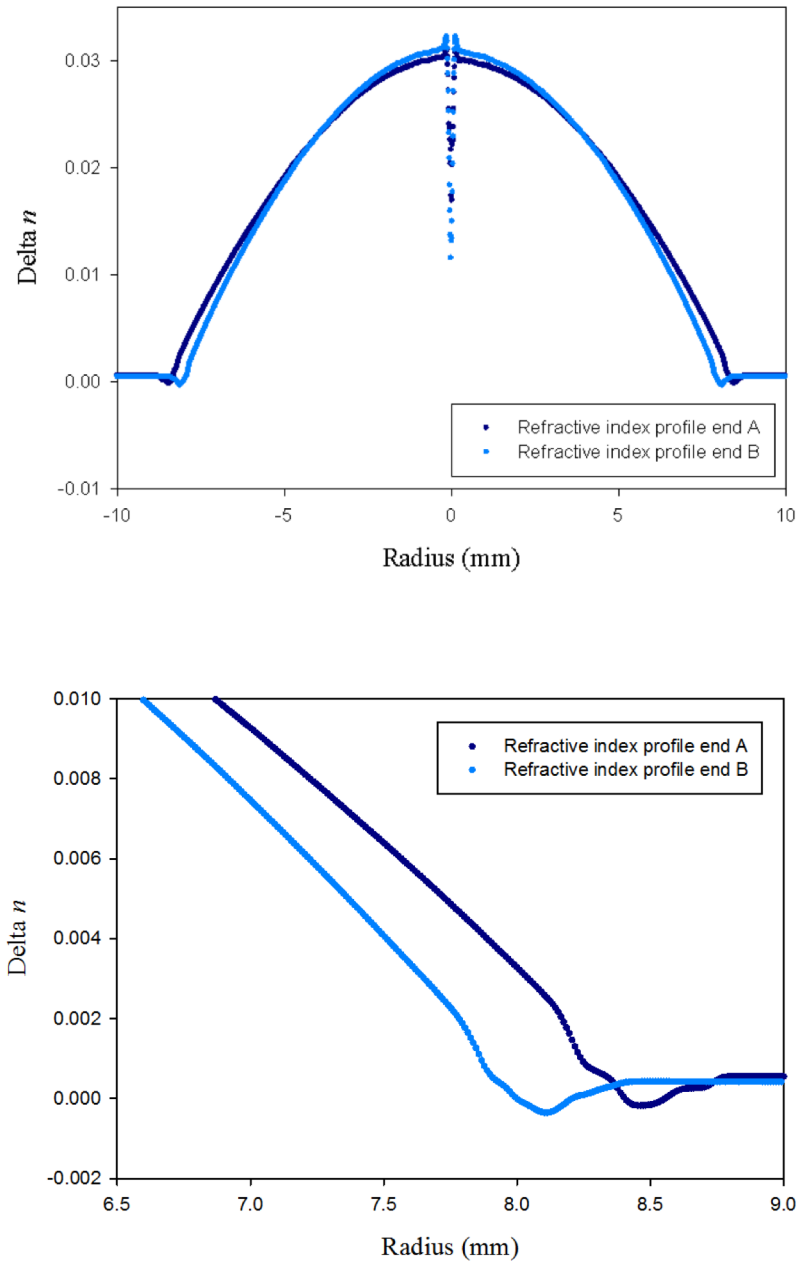

Figure 3.7: Top – The refractive index profile at either end of the supplied Ge-doped rod. Bottom – A closer view of the edge of the dopant region. At closer inspection of the doped region a difference of ~0.5mm in radius is seen over a 1m length. This is a percentage change of ~5.9%.

by an average of 5.3% along the 1m length. This agrees with the estimate of a 4.8% variation in core radii obtained from the measured variation in group index for the $V = 3$ fibre. This residual variation can thus be attributed to non-uniformity in the doped preform used to create the multicore stack. Improving the uniformity of the doping profile along the length of the preform would allow the spread of group indices to be further reduced.

3.4 Mode filter for single mode propagation

At V=3 each of the cores of the fibre is multimode. Figure 3.8 shows the results of a low coherence interferometry measurement from the central core of the V=3

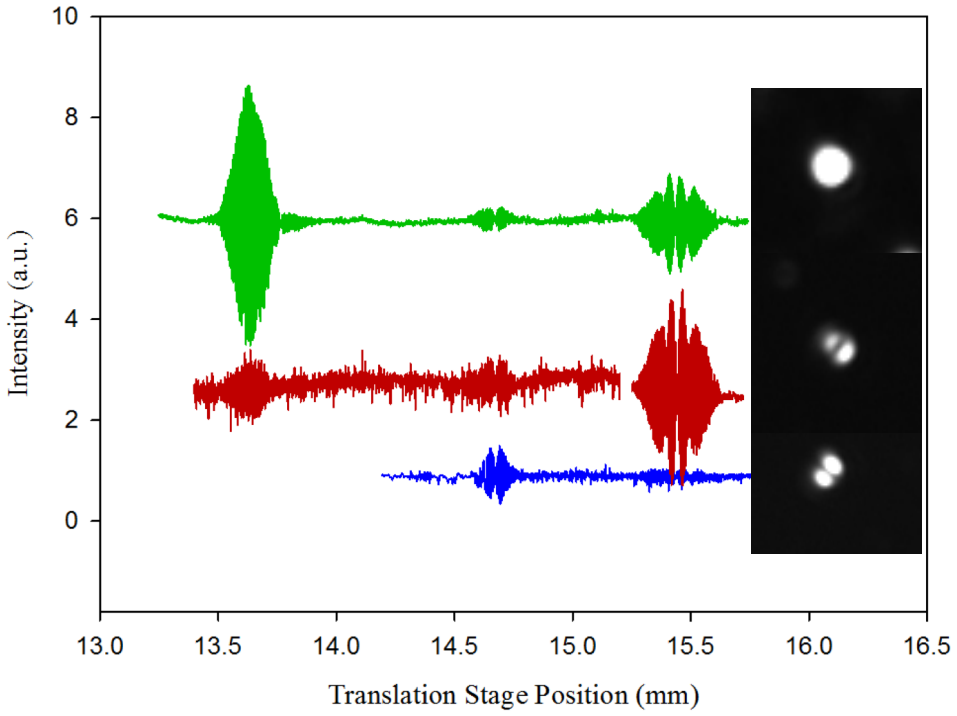

Figure 3.8: Interferogram showing the multiple peaked fringe patterns due to multimode propagation in $V = 3$ fiber together with associated mode profiles. The different coloured curves correspond to different launch conditions for a single fiber core.

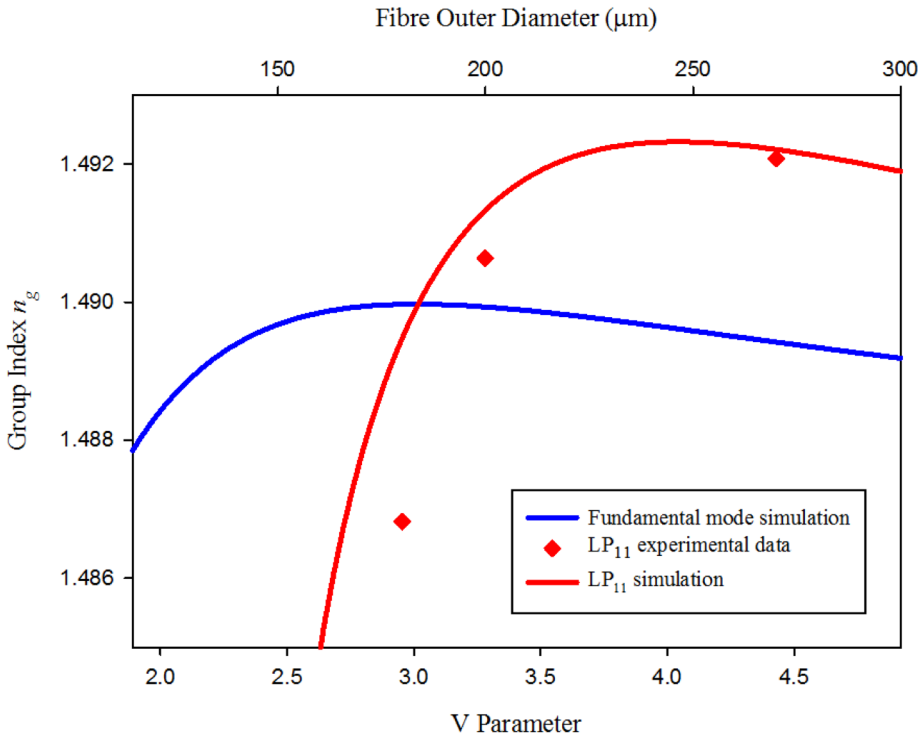

Figure 3.9: Red line – Simulation of the group index for first higher order mode in conjunction with experimentally measured values of group index (red points). Blue line – Simulation of the group index for the fundamental mode.

fibre. As seen from figure 3.8 the higher order modes have different group indices. The differing rates of propagation for each of these modes would prevent a pulse simultaneously injected into each of the cores from fully recombining at the distal end of the fibre. The simulation of the first higher order mode is seen as the red line in figure 3.9. Comparing the simulated values of the group index of the fundamental (blue line) and those of the first mode, a crossing point is seen at $V \approx 3$. From this is might be expected that the presence of this mode would not be a problem, as both modes should have the same group index. However, by inspection, the gradient of the red line at this crossing point is similar to the gradient of the blue fundamental line around the 130µm fibre region. Which, as the previous analysis has shown, results in large variations of the group index. The red points on figure 3.9 represent experimental data points from the central

core of each of the fibres. The difference between the simulated and the experimentally measured value of group index at V=3 can be attributed, in part, to the sensitivity of the group index to core diameter at this point, but it is worth noting that the mode is also approching its cut-off point. It then becomes necessary for to create solely single mode propagation.

In this case a fibre taper is used as a mode filter. By reducing the V value of a section of fibre to below 2.405 where only single mode propagation is allowed then tapering back to the desired outer diameter where group index variation is minimised.

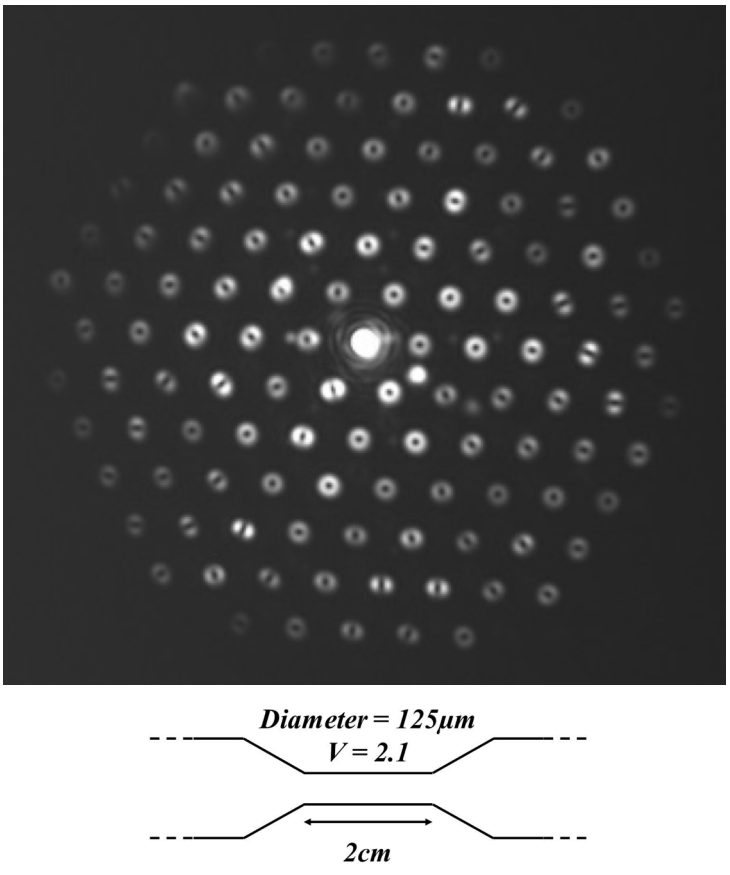

Figure 3.10: Image – Fibre end showing the illumination of the all the cores following the mid-fibre taper (light solely injected into the central core). Schematic of the taper in the centre of the fibre, narrowing from 180µm to 125µm diameter at the waist before transitioning back up to 180µm.

The first taper created utilized a 2cm long waist region of diameter 125µm (V = 2.1, n_g = 1.4887). This was created in the center of the length of the fiber, giving access to both ends for re-cleaving. However, when light was launched into only a single core the output of the fibre was seen across all the cores, imaged in figure 3.10. In the case where the taper is in the centre of the fibre the higher order modes are stripped from the single core (in the down-taper region) but they become modes of the fiber as a whole through the taper waist (as the propagation constants become matched) and are recaptured by the rest of the cores during the up-taper as the propagation constants again match those of the previous regimes. The fiber could be bent at the waist region to help strip away the higher order modes, but this would introduce a group delay across the fiber face. The use of

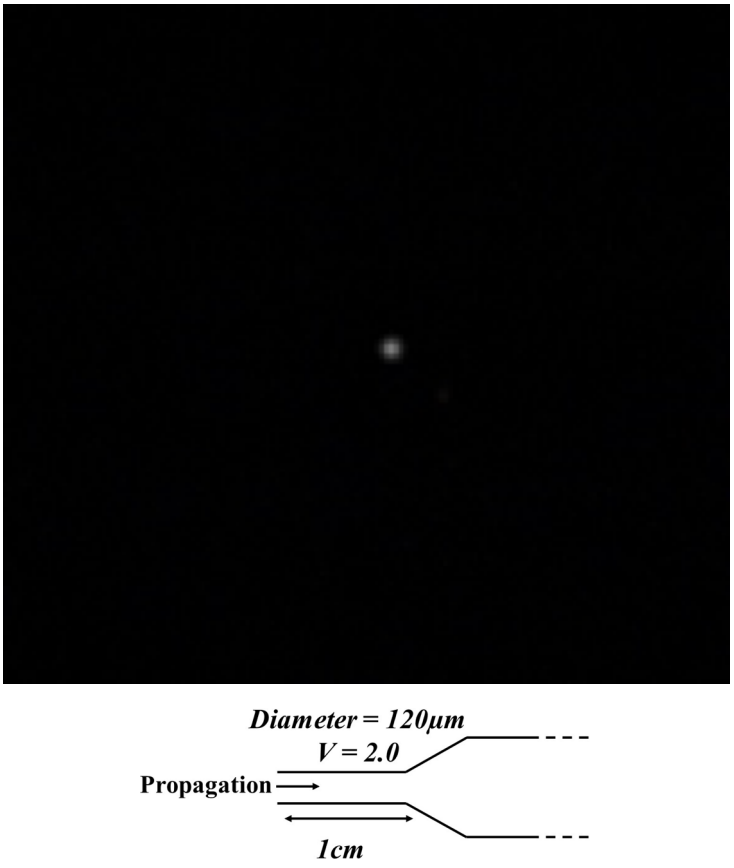

Figure 3.11: Image – Fibre end showing only the central core illuminated after the mode filter (light coupled only into the central core at the input). Schematic of the waist and up-taper region of the fibre.

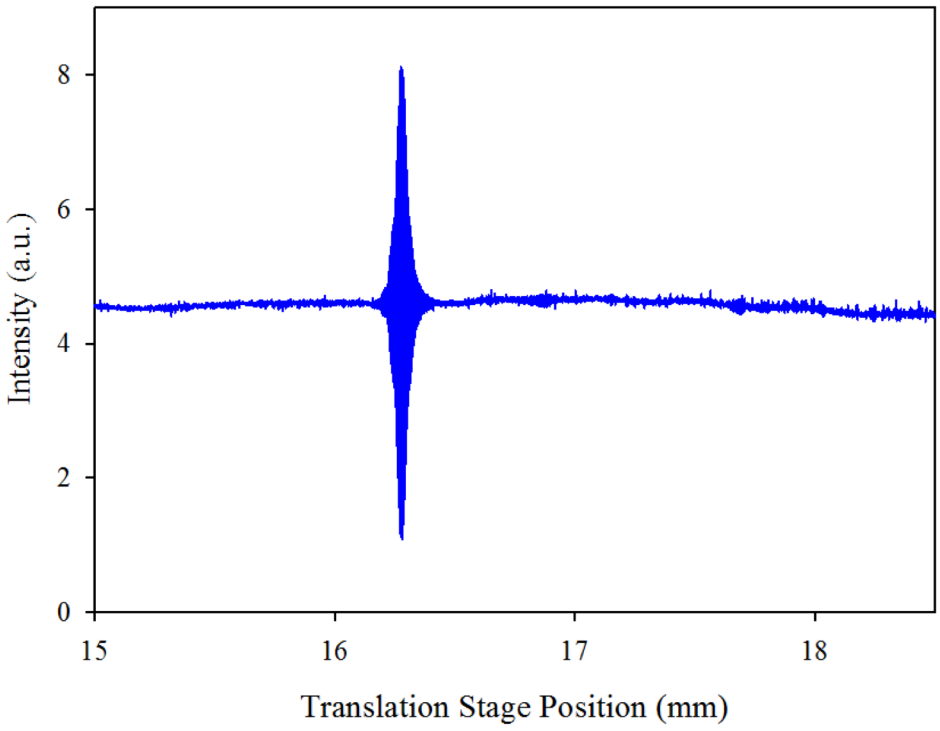

index matching fluids and gels had little noticeable effect of the resulting output face of the fibre.

To avoid the recapturing of modes during the up taper transition the waist of the taper was introduced at the input of the fibre. From the waist region the outer diameter was adiabatically increased from 120µm (where V=2.0, n_g=1.4887) to 180µm (where V=3.0) over a length of 1cm. This means there are no higher modes were not excited and therefore are not present during the up taper to be recaptured. Figure 3.11 shows that all the light is contained within the central input core for this configuration. The same low coherence interferometry was used as with the untapered fibre to verify that the resulting fiber transmitted just the fundamental mode at 800 nm, as illustrated by the interferogram shown in figure 3.12. The presence of a single fringe packet confirms that the taper transmission was adiabatic.

3.5 Conclusion

In this chapter it was demonstrated how, through control of the V parameter, the range of group indices within a multicore fibre was able to be minimized despite any subtle variations in diameter and index contrast from core to core. The optimization found at $V = 3$ would allow 100 fs pulses simultaneous launched into the fibre to be coherently recombined after two meters of propagation. This in turn enables the SLM to create a focused and scannable beam to be formed at the distal end, as required for nonlinear endomicroscopy. It has also been shown that a short tapered region, reducing V to below 2.405 at the proximal end of the multicore fiber, ensures single mode propagation through the subsequent $V = 3$ fiber. This single modedness makes it viable for nonlinear endoscopic imaging.

Chapter 4

Bend insensitive multicore fibre

The work presented in this chapter describes a multicore fibre in which the sensitivity of the phase and group delay between cores of the fibre caused by bends is reduced by spinning the fibre during the draw. Propagation constants of individual cores in the fibre are pre-adjusted as function of their position in the cross section to compensate the additional helical path length inside the spun fibre and match their effective group indices. A comparison between a straight length of fibre and a bent section found that the effect of bending the fibre was reduced by a factor of thirty when compared to an unspun and uniform fibre. This reduction will only improve as the number of bends is increased, as long as the bend circumference of the fibre is sufficiently larger than the spun pitch length.

4.1 Introduction

In vivo nonlinear optical endoscopy has to overcome several problems. The first is the delivery of an ultra-short-pulse excitation laser to the area of interest. Secondly, a mechanism of scanning the laser at a fast enough rate so as to allow for monitoring of biological processes must be employed. A third hurdle is to preserve flexibility in the design.

The preceding chapters have addressed the first two points. However flexing or bending the multicore fibre described previously would cause a delay across the end face of the fibre at the distal end and prevent effective recombination of input pulses.

4.2 Design and fabrication

In a conventional multicore endoscope fibre any bends or turns in the fibre are irrelevant because light is only propagating in a single core at any one time and relative delays have no effect. However bending a multicore fibre introduces a delay to light propagating in cores on the outside of the bend relative to that in the inside cores [87]. As a result, short pulses introduced simultaneously into the different cores will arrive at the distal end at different times. In order to be coherently combined at the distal end and therefore be able to form a useful scanning focal spot, the spread in the pulse arrival times must be within the coherence time. Below it is demonstrated how to design and use a multicore fibre that has reduced sensitivity to bends along the fibre length but in which the cores remains group-index matched, thus potentially enabling a practical endoscopic implementation.

The introduction of the delay to the cores on the outside of the bend is equivalent increasing their group index. Similarly the cores on the inside of the bend would experience an effective decrease in group index when compared to the central core of the fibre. A core following a helical path through the fibre would, when bent, spend as much time on the inside of the bend as it would on the outside of the bend. This averages out the effect of fibre bends, as long as the bent length is sufficiently longer than the helical pitch of the cores inside the fibre. Similarly, spinning the fibre reduces the effect that fibre bending has on the relative phase of light propagating in different cores.

Spinning a multicore fibre with uniform cores will cause those away from the centre to have an increased path length, effectively increasing the group index of those cores. The path length of a particular core over one pitch length is given by

$$P = \sqrt{(2\pi R)^2 + \Lambda^2} \tag{4.1}$$

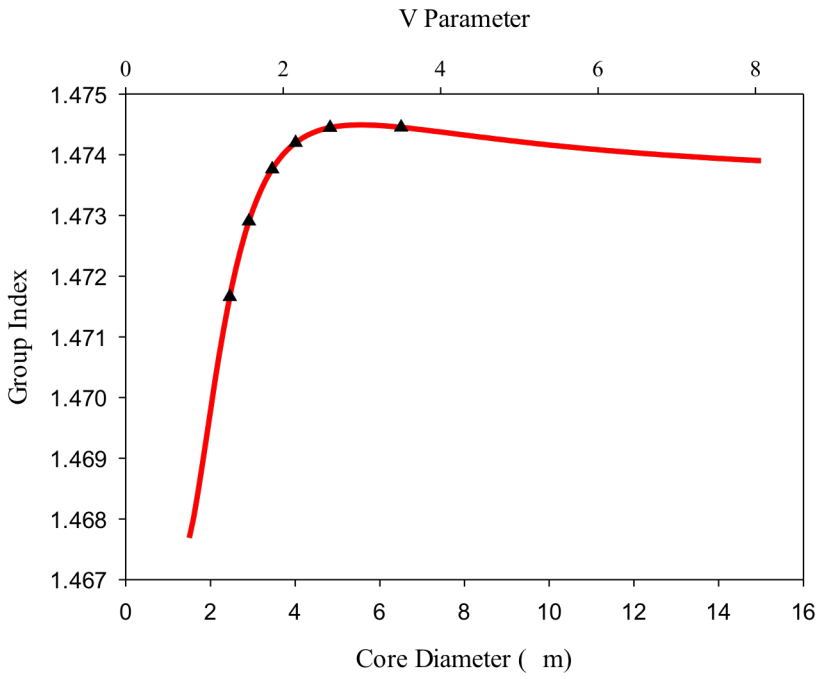

Figure 4.1: Line - numerical calculation of the group index at 800nm for a single step index core of Δ = 0.44%. Points – core diameters for each hexagonal ring of cores, starting from the central core (D = 6.5μm) and moving outwards to the sixth ring (D = 2.4 μm).

where P is the path length, R is the distance of the core from the fibre axis and Λ is the helical pitch of the fibre.

For a pulse to recombine at the output of the fibre all cores must maintain the same optical path length. This can be done by adjusting the (unspun) group index of individual cores by changing the core radius so that the effective group indices are matched when the fibre is spun. Designing a multicore fibre with the central core at V = 3.5, near the peak in group index seen at V=3 in figure 4.1 and adjusting the outer cores to have lower V values allows the effective group index to remain equal across all of the core in the spun fibre despite the different geometric path lengths through the fibre.

Unlike fabricating a typical single or multicore optical fibre this bend insensitive multicore fibre requires the use of additional mechanisms and fabrications techniques.

4.3 Creating the helix

Creating the helical path of the cores within the fibre required the preform to be spun during the fibre draw stage. For this an additional motor was affixed to the chuck which holds the preform as it is drawn. Figure 4.2 shows the added motor, drive belt housing and chuck. Calibration of the rotating chuck found an upper limit of the rotating rate to be 475 r.p.m., figure 4.3. Spinning at this speed however caused the loaded preform to precess strongly within the furnace. The comfortable limit of the rotation with the used preform length and diameter was approximately 300 r.p.m. For the desired helix pitch of 1 cm this put a maximum draw rate of the fibre at 3 m/min.

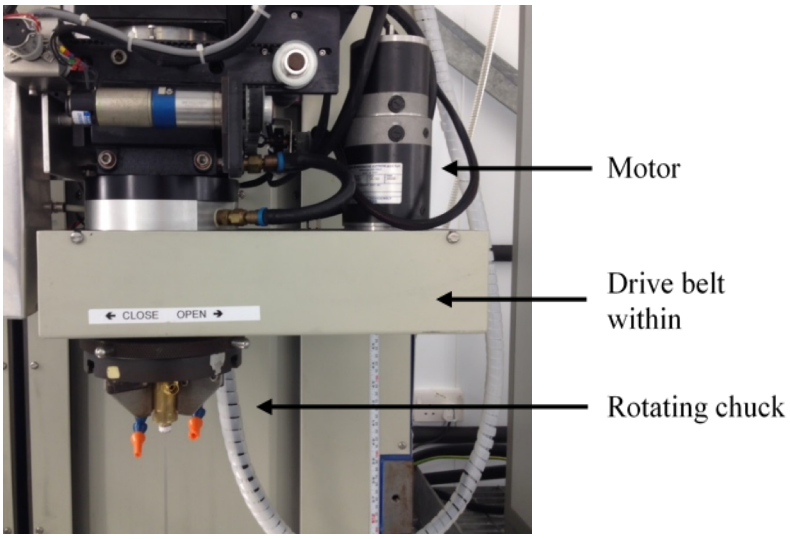

Figure 4.2: The addition of a motor and drive belt to allow rotation of the preform holding chuck. Creating fibre containing cores following helical path lengths.

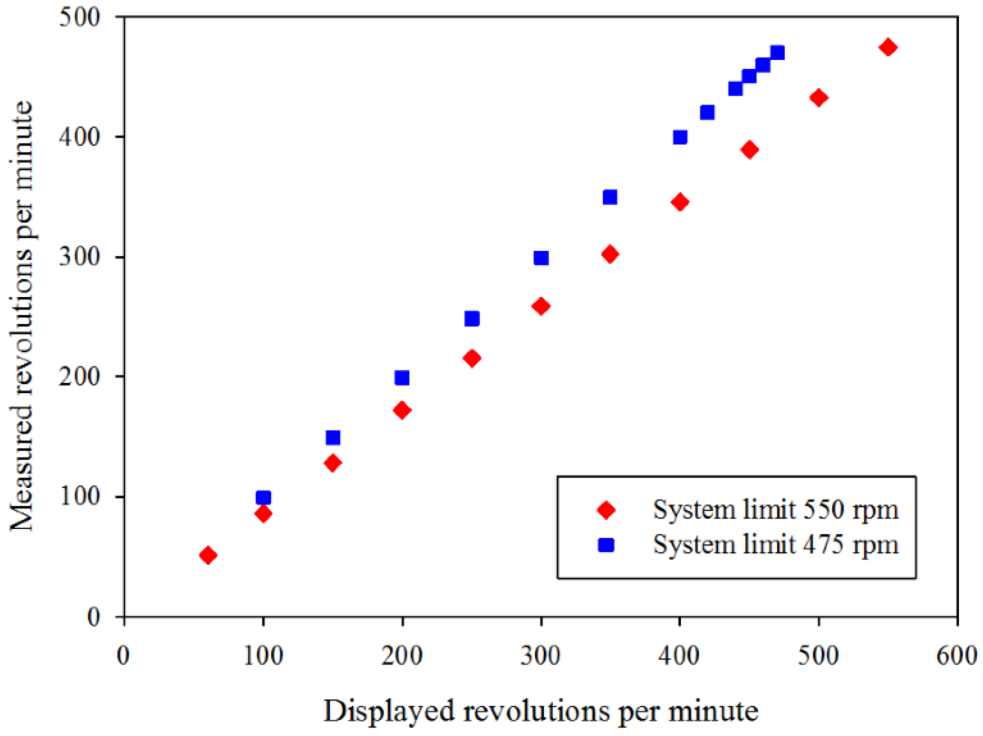

Figure 4.3: Calibration of the rotating chuck was done using hand held revolution counter and adjusting the internal limits of the electronic system.

4.4 Measuring the helical pitch

Confirming the cores within the fibre were in fact following a helical path and measuring the helical pitch was achieved by placing the fibre on its side and adjusting the focus of an optical microscope to a point midway through the fibre where eyelet features are seen to appear at regular intervals as demonstrated in figure 4.4. Comparing the side image of the multicore spun fibre on the left and that of the conventionally drawn multicore fibre on the right hand side of the microscope image in figure 4.4, a different internal structure is clearly seen. The eyelets seen are a result of light being scattered by cores within the fibre moving through the focal plane of the microscope. It is unclear whether the eyelet pattern

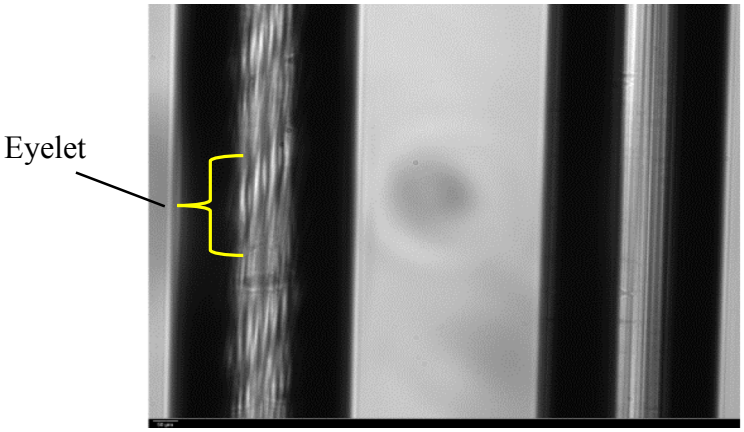

Figure 4.4: Comparison between a helical section of fibre (left) and an unspun section of the same design (right). The helical fibre shows eyelets at regular intervals, which can be used to measure the helical pitch of the optical fibre.

is caused by the flat edges of the hexagon or the corners, but the hexagonal nature of the stacked cores means that counting six of these features along the fibre length allows the helical pitch to be measured in a reliable manor.

4.5 Fabricating a constant core-core pitch

The range of proposed core diameters within the spun fibre means that maintaining a constant core-core pitch across the fibre face requires specific jacketing of each core. The central core, being the largest, should have the thinnest jacketing tube and the outermost cores will have the thickest jacket. Ultimately giving the same core separation throughout the fibre.

Parameters surrounding the design of the helical fibre, such as helix or core-core pitch, were adjusted in a bid to cause the six different jacket seizes necessary to fall within the range readily available from the glass stock. In some instances it became necessary to slightly alter the inner diameter to outer diameter ratio (ID/OD ratio).

4.6 Controlling the ratio using temperature

Using the cane drawing tower a tube with initial outer diameter of 25 mm and inner diameter of 21 mm was pressurised to 1 kPa. The tube was then draw down to a constant diameter of 1.6 mm whilst the temperature of the furnace was increased from 1960 °C to 2040 °C. During the draw the draw speed was adjusted to maintain the 1.6 mm diameter. From figure 4.5 an obvious increase in draw speed is seen from 0.607 m/min at 1960 ^{o}C to 0.677 at 2030 ^{o}C. This increase in draw speed but constant outer diameter suggests that the wall thickness must be decreasing, the glass entering and exiting the furnace must to be conserved. As seen from the blue points in figure 4.6 the drawn jacket ID/OD ratio changes from 0.826 to 0.854 (the original ratio of the input tube was 0.840) as expected.

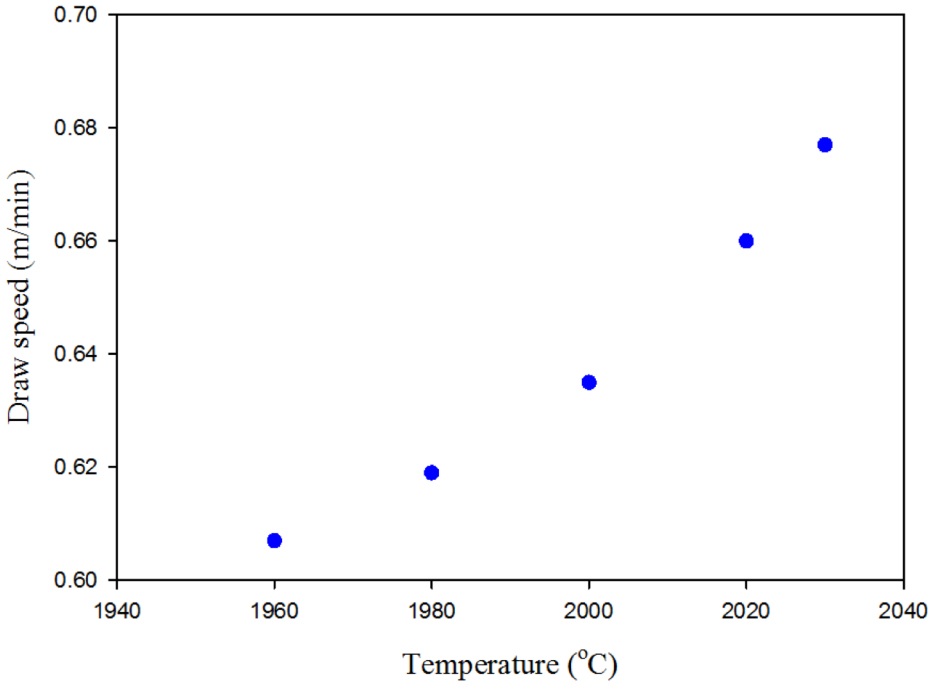

Figure 4.5: The draw speed required to maintain a constant outer diameter of a drawn cane (at constant feed rate and pressure) as the temperature of the furnace was increased from 1960 ^{o}C to 2030 ^{o}C.

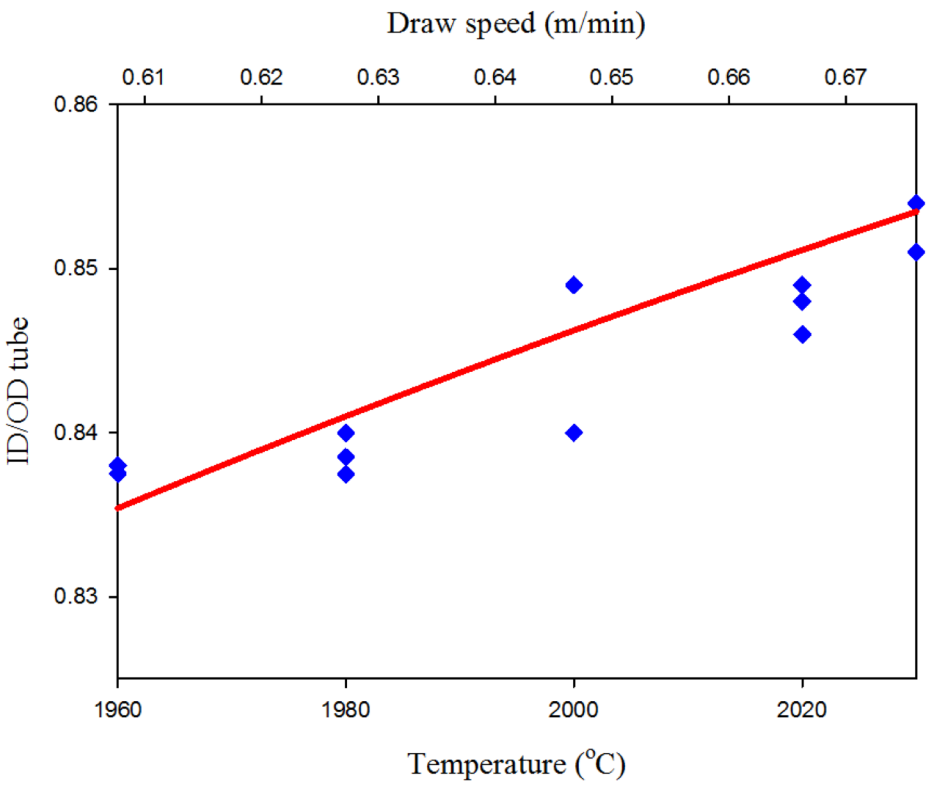

Figure 4.6: Red line – Calculated ID/OD ratio for a constant feed rate and drawn outer diameter for a given input tube of ratio 0.84. Blue points – Experimentally measured ratios at each temperature for drawn tubes of the same outer diameter.

The red line represents a calculated ID/OD ratio for a particular draw speed (for constant input feed rate and tube diameters as well as constant output outer diameter) using equation 4.2

$$IN = F \times \left[\left(\frac{OD_1}{2} \right)^2 - \left(\frac{ID_1}{2} \right)^2 \right] \times \square$$

$$OUT = D \times \left[\left(\frac{OD_2}{2} \right)^2 - \left(\frac{ID_2}{2} \right)^2 \right] \times \square$$

$$D = F \times \frac{(OD_1^2 - ID_1^2)}{(OD_2^2 - ID_2^2)} \qquad 4.2$$

where F is the feed rate, D is the draw speed and ID and OD are the inner and outer diameters respectively.

4.7 Controlling the ratio using pressure

Adjusting the wall thickness (and subsequently the ID/OD ratio) through the control of pressure differences inside and outside of the drawn tube was done at a constant furnace temperature of 2020°C. Again, the cane drawing tower was used along with a tube of initial outer diameter of 25 mm and inner diameter of 21 mm. The tube was then draw down to a constant diameter of 1.6 mm whilst the pressure inside the tube was increased from 0.1 kPa to 2 kPa. Maintaining an input feed rate of 2 mm/min during the pressure changes required the draw speed to be increased from 0.526 to 0.686 m/min. Within this pressure range a clear relationship is seen in figure 4.7 between the applied pressure and draw speed.

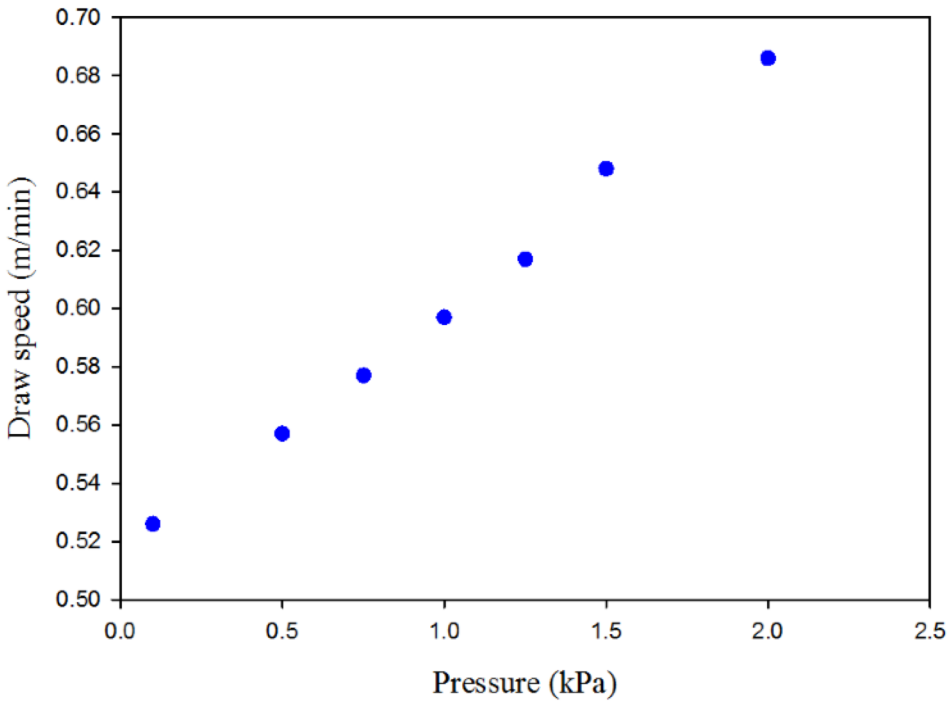

Figure 4.7: The draw speed required to maintain a constant outer diameter of a drawn cane (at constant feed rate and temperature) as the pressure of the furnace was increased from 0.1kPa to 2kPa.

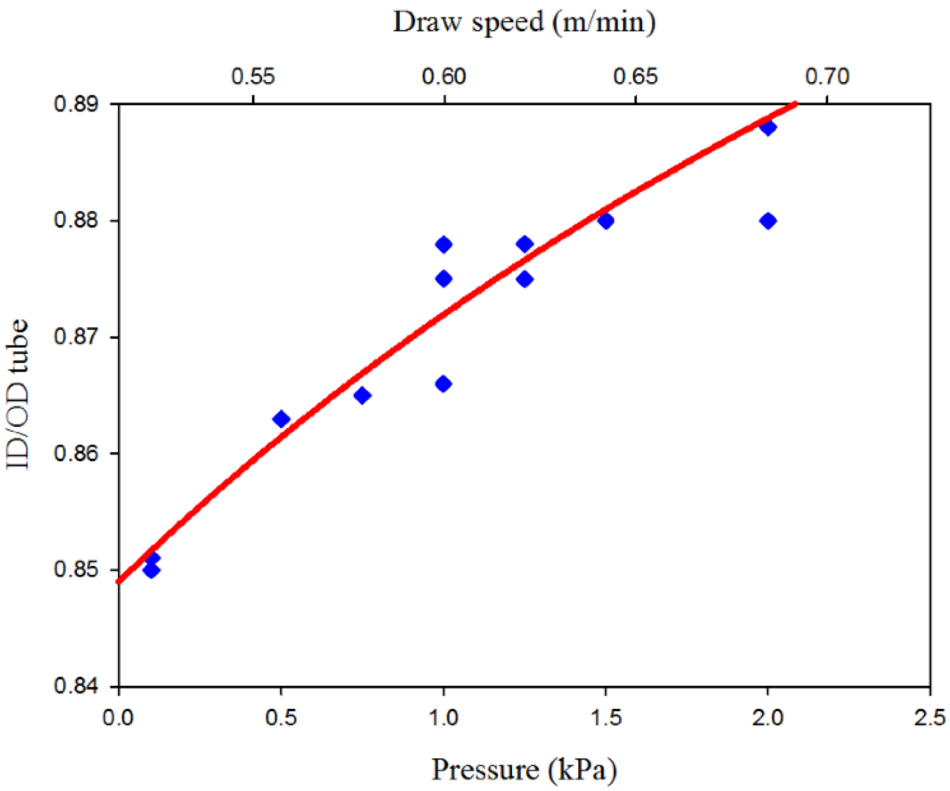

Figure 4.8: Red line – Calculated ID/OD ratio for a constant feed rate and drawn outer diameter for a given input tube of ratio 0.84. Blue points – Experimentally measured ratios at each pressure for drawn tubes of the same outer diameter.

As previously stated, from equation 4.2, the necessary increase in draw speed to maintain a constant outer diameter of 1.6 mm must result in a decrease in wall thickness (increase in ID/OD ratio). At each pressure stage the wall thickness was measured by an optical microscope. The results of the measurements can be seen in figure 4.8 as the blue diamonds (expressed as the ID/OD ratio). The expected calculated values of the ID/OD ratio is shown as the red line passing through the cluster of experimentally gathered points.

Looking at the results of the cane drawing experiments a level of control is available in ID/OD ratio. The magnitude of the changes measured (despite being, at most, less than a 6% change) provide a slightly wider window for the design parameters of the helical multicore fibre.

4.8 Effect on group index of spinning the fibre

As already discussed spinning the fibre to create the helical paths of the cores will increase the effective group index from the increased path length. However, each core following the helix will have as a result a radius of curvature. The effect of this on the refractive index can be represented by a slope (calculable from the radius of curvature) as seen in figure 4.9. This change in the effective refractive index profile does result in a change in the group index of the core at larger core sizes as demonstrated in figure 4.10. Qualitatively this makes sense; as the core size increases the mode will shift more and more towards the elevated region of

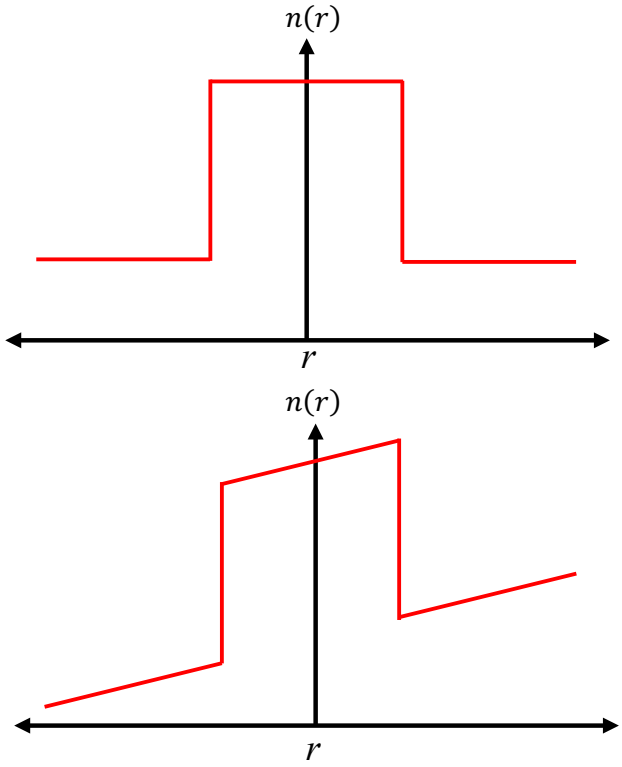

Figure 4.9: Refractive index profiles across the core of a straight step index fibre (top). Effective index profile across a step index core when bent.

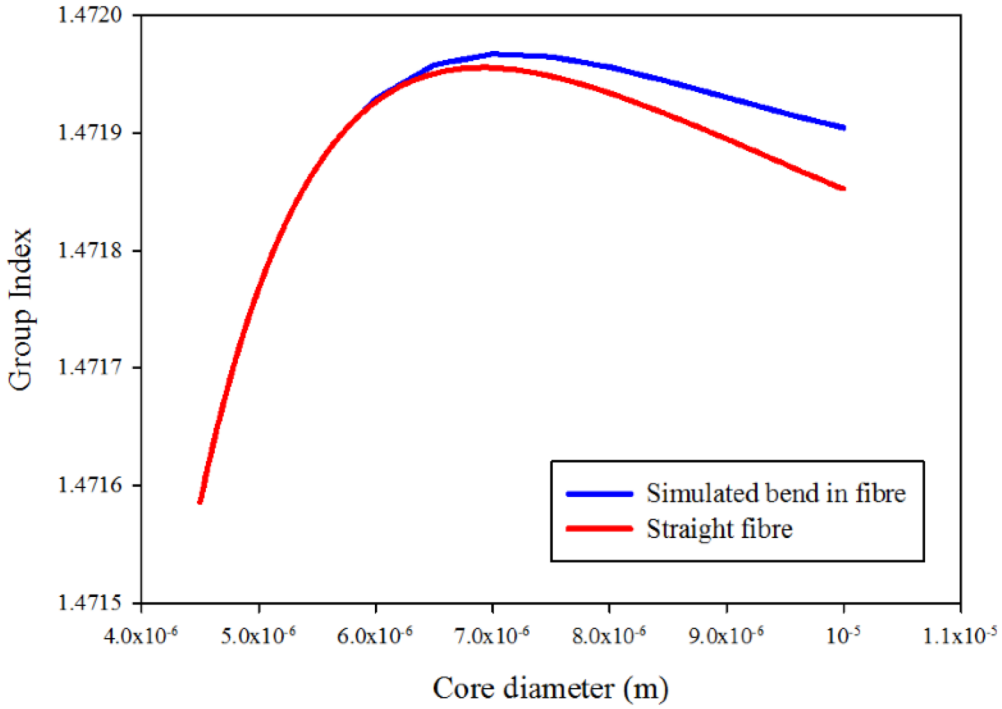

Figure 4.10: Comparison of the group index for a straight section of fibre and for a fibre experiencing a bend of radius of 15 mm. It is worth noting that in the fibre fabricated the outer ring of cores experienced a bend radius of 23.1 mm, meaning that the result above is more pronounced than in the fabricated fibre.

refractive index, in turn, increasing the group index. On the left hand side of the peak the group index the two refractive index profiles lie on top of each other.

This allows the effect to be ignored as long as the fibre is fabricated using the small core diameter edge of the group index curve.

4.9 Producing the helical fibre

The techniques outlined above were employed to create a 91-core multicore preform. Each step index core used the same index step $\Delta = 0.44\%$. Each hexagonal ring of cores was approximated as a circle with a radius given by the average distance of that hexagonal ring from the central core. The helical pitch of the fibre was selected to be 10 mm and the core-core pitch was 22 µm. The

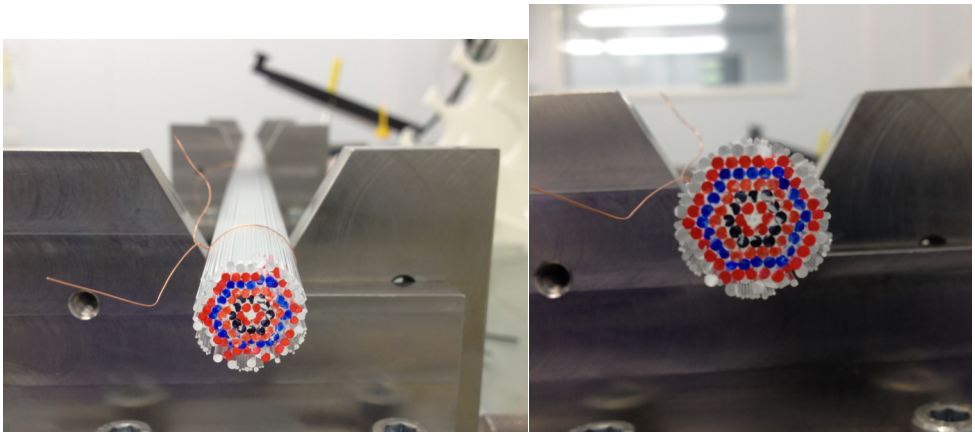

Figure 4.11: An interim stage in the stack and draw process. Each of the 91 cores are suitably jacketed and stacked, with the coloured ends corresponding to the different core sizes throughout the stack.

total number of cores, and the pitches within the fibre were chosen so that the group indices necessary for equal optical path lengths were within the possible fabrication boundaries and outside of significant core-core coupling range. From these values of core-core pitch and helical pitch the necessary group index and associated core radius was calculated for each ring of cores to equalize the effective group indices in the final spun fibre, seen as the black points in figure

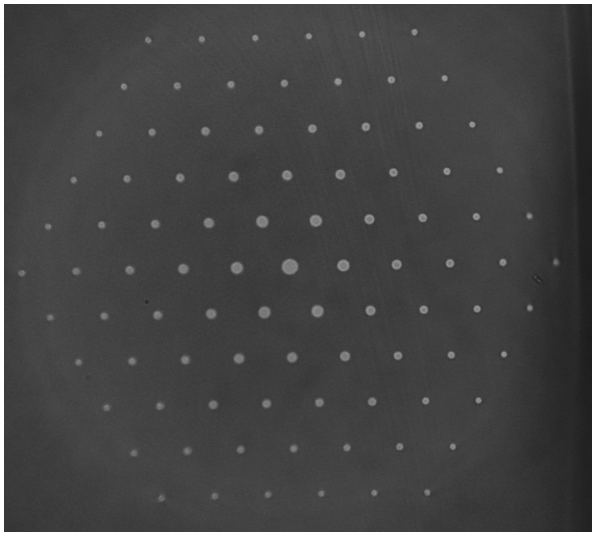

Figure 4.12: Multicore fibre end face showing decreasing core radius towards the edge of the fibre.

4.1. Intermediate stages of the fabrication process and the final fibre image are seen in figure 4.11 and 4.12 respectively.

4.10 Experiment and results

A fibre-based optical supercontinuum was used as a low-coherence light source for a scanning Mach-Zehnder interferometer. A 10 nm bandpass filter selected a central wavelength of 800 nm. As before translation stages were used to move the input and output of the sample fibre so as to study different cores. Moving the fibre ends rather than the lenses ensured that the optical path outside of the fibre was identical from measurements of one core to another.

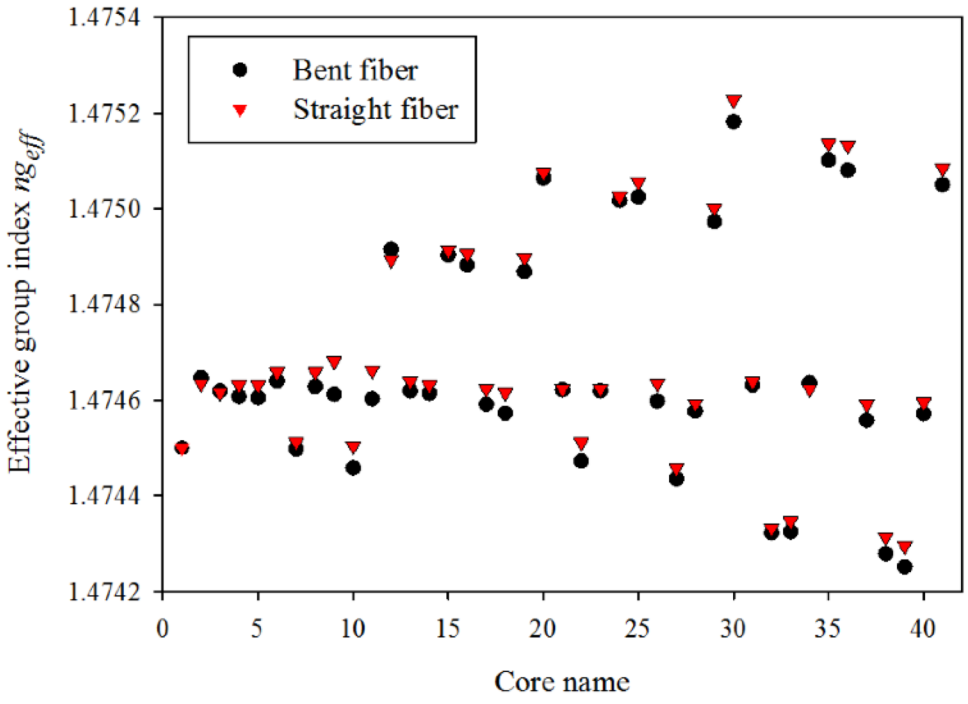

Figure 4.13: Variation in effective group index for each of the 41 cores measured in the straight fiber (triangles) and in the three times turned fiber (circles).

The effective change in group index across the cores in the fibre was measured in two arrangements, a completely straight length of fibre and then a length of fibre with three loops of 6.4 cm diameter. Exactly the same 'bow tie' configuration of 41 cores (figure 4.15) was measured in each case to provide a sample of the whole fibre.

Figure 4.13 shows the effective group index measured across the 41 cores for both the straight and the bent fibre. In the bent fibre, an effective change in group index of 1.04×10^{-3} would be expected between an outer core and the central core, for a uniform unspun multicore fibre of the same core-core pitch. The maximum shift in effective group index would be across the full face of the fibre, double the value above. The maximum bend-induced shift in effective group

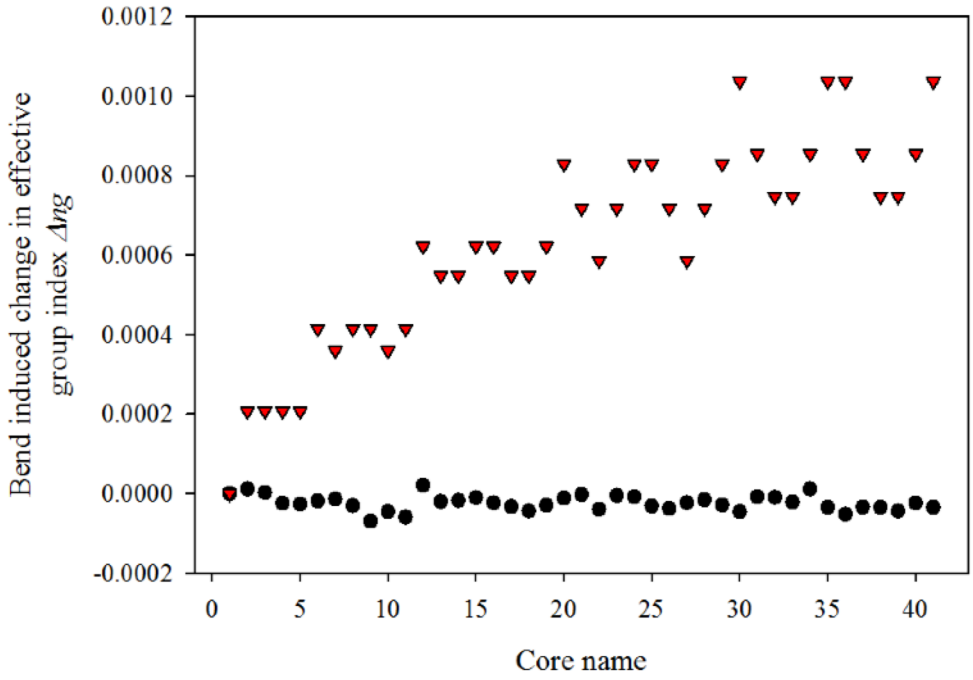

Figure 4.14: The effective group index shift due to bending calculated for a uniform unspun multicore fiber (red triangles) and that measured in the specially designed spun fiber (black circles) over three loops of 6.4 cm in diameter. It is worth noting that the shift calculated for the unspun fiber is with respect to the central core, the total group index discrepancy across the entire fiber end face would be double that shown.

index seen by a core in the spun fibre (core 9) is 7.0×10^{-5}, 30 times less. Figure 4.14 clearly shows the comparative sizes of the group index shift expected for a uniform unspun multicore fibre (red triangles) and that measured in the specially designed spun fibre (black circles). The expected shift for the uniform unspun fibre was calculated by assuming that each core was in the same plane as the fibre loops.

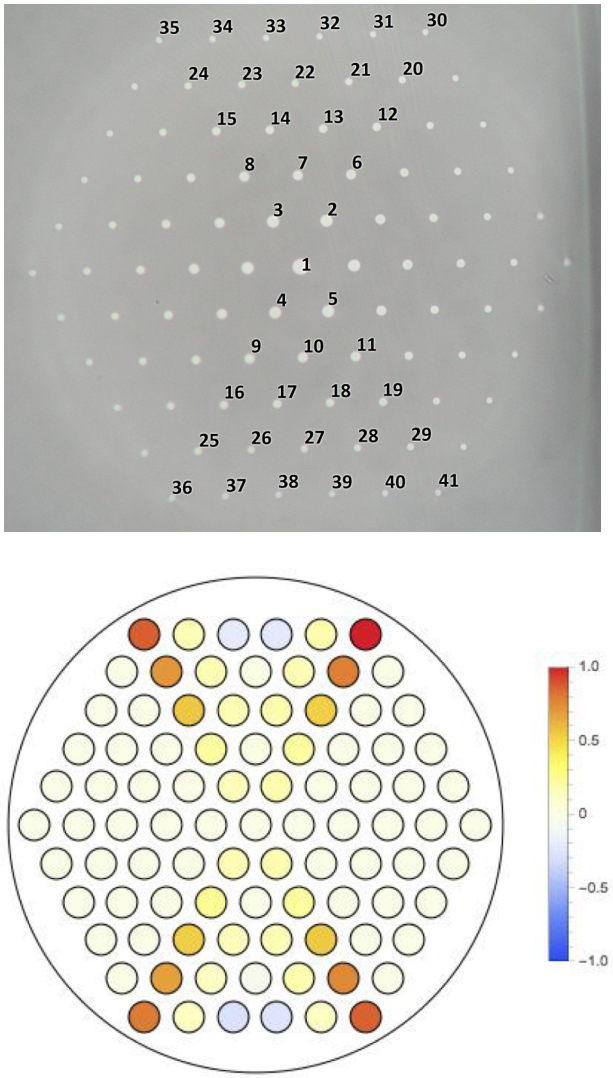

Figure 4.15: Top – 'Bow tie' selection of cores measured. Bottom - A normalized 'heat map' showing cores with larger positive change in group index compared to the central core in deepening red and negative changes in blue.

A bandwidth limited pulse centred at 800 nm (band and temporal widths 10 nm and 94 fs respectively) requires a change in effective group index of less than 0.000028 between cores to coherently recombine after propagation through 1m of fibre. In both the straight and bent fibre cases, 48% of the measured cores fall within this boundary. A longer pulse length of 300 fs would allow two thirds (65%) of the measured cores to fall within this boundary, it is worth noting here that the cores lying outside this boundary are the same in both fibre arrangements.

Looking more closely at the effective changes in group index and specifically at the largest outliers, cores 12, 15, 16, 19, 20, 24, 25, 29, 30, 35, 36, 41. These cores are those on the corners of their rings. From this it is clear that the current limiting factor is the approximation of the hexagonal arrangement of cores as a circle. At the corners this approximation is most pronounced and clearly shows up in figure 4.13 as three distinct groups of four above the main bunch (top) and as the most darkly coloured cores (bottom). The geometrical path length is longer than for the cores situated on the straight edges, leading to an increase in optical path length and apparent increase in overall effective group index.

4.11 Conclusion

We have demonstrated how, through careful design of the individual cores in a spun multicore fibre, the differential delay introduced to different cores through bending can be reduced. Through our fibre 100 fs pulses simultaneously launched would be able to coherently recombine after 1 m of propagation to form a focused scanning spot without requiring the fibre to be straight.

A possible method to reduce further the measured group index spread would be by calculating the core diameters needed for an equal optical path length for each individual core. This is instead of approximating each hexagonal ring as a circle of average radius, this would prevent the corners forming the outliers, as they did in this case.

Chapter 5

Conclusions and the future

In this thesis the fabrication and design of multicore optical fibres has been explored with a view to improve *in vivo* medical nonlinear imaging techniques. Novel fibres have been created and new fabrications methods revealed.

In chapter 3 a method of uniforming the group indices of cores within a multicore fibre was investigated. The group index variation was found to be minimised at a V value of three. Improvements to the fabricated fibre could be made with more uniformly doped rods to start the process and by increasing the total number of cores within the fibre.

In chapter 4 novel fabrication methods were explored to solve the problem of bending causing a group delay across the face of a multicore fibre. The solution of using a helical path through the fibre by the constituent cores was found to be successful. Better path length compensation (through more specific control of individual core group indices) would improve the spread of measured effective indices.

Alternative strategies for nonlinear endoscopy chiefly involve the use of a mechanical element at the distal end. These elements can be very small, an example being the work by M. Gu et al. where a double clad PCF uses a microelectromechanical system (MEMS) mirror. The component size in this case is just 2.7x1.9x1.2mm, however this is still large compared to the tip of an optical fibre. The greater size of the mechanical tips does allow for larger possible areas to be analysed in a single instance.

The work in this thesis provides only a step towards *in vivo* nonlinear imaging becoming a routine practice within medical imaging. I look forward to seeing the field continue its rapid progression towards more useful and informative imaging systems.

References

[1] A. Yariv. Optical Electronics in Modern Communications. Bibliographical Society, 1997.

[2] W. Snyder and R. A. Sammut, "Fundamental (HE_{11}) Modes of Graded Optical Fibers," Journal of the Optical Society of America, 69:1663-1671, 1980.

[3] H. Matsumura and T. Suganuma, "Normalization of Single-Mode Fibers Having an Arbitrary Index Profile," Applied Optics, 19:3151-3158, 1980.

[4] A. Millar, "Direct Methods of Determining Equivalent Step-Index Profiles for Monomode Fibers," Electronics Letters, 17:458-460, 1981.

[5] J. C. Maxwell. A Dynamical Theory of the Electromagnetic Field. Roy. Soc. Trans., CLV:459, 1865.

[6] Gloge, "Dispersion in weakly guiding fibers," Applied Optics, 10:2242-2245, 1971.

[7] D. Davidson, ''Single-Mode Wave Propagation in Cylindrical Optical Fibers'', in E. E. Basch (ed.), *Optical Fiber Transmission,* Howard W. Sams, Indianapolis , 27–64. 1987

[8] Senior J.M. Optical Fibre Communications: Principles and Practice 2nd edition. Prentice Hall Europe. 1992.

[9] Agrawal G.P. Nonlinear Fibre Optics 4th edition. Academic Press, Elsevier. 2007.

[10] W. J. Stewart and J. D. Love. "Design limitation on tapers and couplers in single mode fibres," in Proc. ECOC '85 (Venice), pp. 559-562. J. D. 1985.

[11] J. D. Love and W. M. Henry, "Quantifying loss minimisation in single mode fibre tapers, "Electron. Lett., 22:912-914. 1986.

[12] T. A. Birks and Y. W. Li, "The shape of fiber tapers", J. Lightwave Technol. 10, 432 (1992).

[13] T. A. Birks et al., "Supercontinuum generation in tapered fibers", Opt. Lett. 25 (19), 1415 (2000).

[14] Benabid, F., 2006. Hollow-core photonic bandgap: new light guidance for new science and technology. *Phil. Tran. of the Roy. Soc. A*, 364, 3439-3462

[15] K. Mukasa, K. Imamura, Y. Tsuchida and R. Sugizaki, "Multi-Core Fibers for Large Capacity SDM" Proceedings of Optical Fiber Communication/National Fiber Optic Engineers Conference, Los Angeles, United States, March 2011.

[16] K. Takenaga, S. Tanigawa, N. Guan, S. Matsuo, K. Saitoh, and M. Koshiba, "Reduction of crosstalk by quasi-homogeneous solid multi-core fiber," Optical Fiber Communication Conference and National Fiber Optic Engineers Conference (OFC/NFOEC 2010), 2010, OWK7.

[17] M. Koshiba, "Recent Progress in Multi-Core Fibers for Ultra-large Capacity Transmission" Proceedings of OptoElectronics and Communications Conference (OECC2010), Sapporo Convention Center, Japan, July 2010, pp. 38-39.

[18] M. Koshiba, K. Saitoh and Y. Kokubun, "Heterogeneous Multi-Core Fibers: Proposals and Design Principles" IEICE Electronics Express, Vol. 6, No. 2, pp. 98-103.

[19] Sebastian Dochow, Ines Latka, Martin Becker, Ron Spittel, Jens Kobelke, Kay Schuster, Albrecht Graf, Sven Brückner, Sonja Unger, Manfred Rothhardt, Benjamin Dietzek, Christoph Krafft, and Jürgen Popp, "Multicore fiber with integrated fiber Bragg gratings for background-free Raman sensing," Opt. Express 20, 20156-20169 (2012).

[20] J. M. Stone, F. Yu, and J. C. Knight, "Highly birefringent 98-core fiber," Opt. Lett. 39, 4568-4570 (2014).

[21] F. Helmchen and W. Denk. Deep tissue two-photon microscopy. Nat. Methods, 2:932:940, 2005.

[22] B. Brown, R. B. Campbell, Y. Tsuzuki, L. Xu, P. Carmeliet, D. Fukumura, and R. K. Jain. In vivo measurement of gene expression, angiogenesis and physiological function in tumors using multiphoton laser scanning microscopy. Nat. Medicine, 7:864:868, 2001.

[23] R. K. Jain, L. L. Munn, and D. Fukumura. Dissecting tumor pathophysiology using intravital microscopy. Nat. Rev. Cancer, 2:266:275, 2002.

[24] J. Condeelis and J. E. Segall. Intravital imaging of cell movement in tumors. Nat. Rev. Cancer, 3:921:930, 2003.

[25] W. R. Zipfel, R. M. Williams, and W. W. Webb. Nonlinear magic: multiphoton microscopy in the biosciences. Nat. Biotech., 21:1369:1377, 2003.

[26] C. Xu, W. Zipfel, J. B. Shear, R. M. Williams, and W. W. Webb. Multiphoton fluorescence excitation: New spectral windows for biological nonlinear microscopy. Proc. Natl. Acad. Sci. USA, 93:10763:10768, 1996.

[27] P. J. Campagnola, M. Wei, A. Lewis, and L. M. Loew. High-resolution nonlinear optical imaging of live cells by second harmonic generation. Biophys. J., 77:3341 :3349, 1999.

[28] P. J. Campagnola, A. C. Millard, M. Terasaki, P. E. Hoppe, C. J. Malone, and W. A. Mohler. Three-dimensional high-resolution second-harmonic generation imaging of endogenous structural proteins in biological tissues. Biophys. J., 81:493:508, 2002.

[29] P. J. Campagnola and L. M. Loew. Second harmonic imaging microscopy for visualizing biomolecular arrays in cells, tissues and organisms. Nat. Biotech., 21:1356:1360, 2003.

[30] Y. R. Shen. The Principles of Nonlinear Optics. J. Wiley, New York, 1984.

[31] J. X. Cheng and X. S. Xie. Coherent anti-stokes Raman scattering microscopy: Instrumentation, theory, and applications. J. Phys. Chem. B, 108:827:840, 2004. 147 Bibliography

[32] T. Yeh, N. Nassif, A. Zoumi, and B. J. Tromberg. Selective corneal imaging using combined second-harmonic generation and two-photon excited fluorescence. Opt. Lett., 27:2082:2084, 2002.

[33] Zoumi, A. Yeh, and B. J. Tromberg. Imaging cells and extracellular matrix in vivo by using second-harmonic generation and two-photon excited fluorescence. Proc. Natl. Acad. Sci. USA, 99:11014:11019, 2002.

[34] W. E. Zipfel, R. M. Williams, R. Christie, A. Y. Nikitin, B. T. Hyman, and W. W. Webb. Live tissue intrinsic emission microscopy using multiphoton-excited native fluorescence and second harmonic generation. Proc. Natl. Acad. Sci. USA, 100:7075:7080, 2003.

[35] Zoumi, X. Lu, G. S. Kassab, B. J. Tromberg. Imaging coronary artery microstructure using second-harmonic and two-photon fluorescence microscopy. Biophys. J., 87:2778:2786, 2004.

[36] Helmchen, M. S. Fee, D. W. Tank, W. Denk. A miniature head-mounted two-photon microscope: High-resolution brain imaging in freely moving animals. Neuron, 31:903:912, 2001.

[37] D. Bird and M. Gu. Compact two-photon fluorescence microscope based on a single-mode fiber coupler. Opt. Lett., 27:1031:1033, 2002.

[38] D. Bird and M. Gu. Two-photon fluorescence endoscopy with a micro-optic scanning head. Opt. Lett., 28:1552:1554, 2003.

[39] J. C. Jung and M. J. Schnitzer. Multiphoton endoscopy. Opt. Lett., 28:902:904, 2003.

[40] W. Gobel, J. N. D. Kerr, A. Nimmerjahn, and F. Helmchen. Miniaturized twophoton microscope based on a flexible coherent fiber bundle and a gradient-index lens objective. Opt. Lett., 29:2521:2523, 2004.

[41] M. T. Myaing, D. J. MacDonald, and X. Li. Fiber-optic scanning two-photon fluorescence endoscope. Opt. Lett., 31:1076:1078, 2006. 148 Bibliography

[42] P. Agrawal. Nonlinear Fiber Optics. Academic, San Diego, 1989.

[43] Dabbs, T. & Glass, M. (1992) Fibre-optic confocal microscope: FOCON. *Appl. Opt.* **31**, 3030–3035.

[44] Gobel, W., Kerr, J.N.D., Nimmerjahn, A. & Helmchen, F. (2004b) Miniaturized two-photon microscope based on a flexible coherent fiber bundle and a gradient-index lens objective. *Opt. Lett.* **29**, 2521–2523.

[45] Helmchen, F., Fee, M.S., Tank, D.W. & Denk,W. (2001) A miniature headmounted two-photon microscope: High-resolution brain imaging in freely moving animals. *Neuron*. **31**, 903–912.

[46] Kim, D., Kim, K.H., Yazdanfar, S. & So, P.T.C. (2005) Optical biopsy in high-speed handheld miniaturizedmultifocalmultiphoton microscopy. *Multiphoton Microscopy in the Biomedical Sciences V* (ed. by A. Periasamy

[47] M. V. Iravani. Fibre-optic scanning differential interference contrast optical microscope. Electron. Lett., 22:103:105, 1986.

[48] R. Rouse, A. Kano, J. A. Udovich, A. M. Kroto, A. F. Gmitro. Design and demonstration of a miniature catheter for a confocal microendoscope. Appl. Opt., 43:5763:5771, 2004.

[49] W. Kaiser, C. G. B. Garrett. Two-photon excitation in CaF2:Eu3+. Phys. Rev. Lett., 7:229:231, 1961.

[50] S. Singh and L. T. Brandley. Three-photon absorption in napthalene crystals by laser excitation. Phys. Rev. Lett., 12:612:614, 1964.

[51] W. Denk, J. H. Strickler, and W. W. Webb. Two-photon laser scanning fluorescence microscopy. Science, 248:73:75, 1990.

[52] S. Maiti, J. B. Shear, R. M. Williams, W. R. Zipfel, and W. W. Webb. Measuring serotonin distribution in live cells with three-photon excitation. Science, 275:530:532, 1997. 149 Bibliography

[53] R. M. Williams, J. B. Shear, W. R. Zipfel, S. Maiti, and W. W. Webb. Mucosal mast cell secretion processes imaged using three-photon microscopy of 5-hydroxytryptamine autouorescence. Biophys. J., 76:1835:1846, 1999.

[54] S. W. Hell, K. Bahlmann, M. Schrader, A. Soini, H. Malak, I. Gryczynski, and J. R. Lakowicz. Three-photon excitation in fluorescence microscopy. J. Biomed. Opt., 1:71:74, 1996.

[55] X. Gan and M. Gu. Fluorescence microscopic imaging through tissue-like turbid media. J. Appl. Phy., 87:3214:3221, 2000.

[56] M. Gu, X. Gan, A. Kisteman, and M. G. Xu. Comparison of penetration depth between two-photon excitation in imaging through turbid tissue media. Appl. Phys. Lett., 77:1551:1553, 2000.

[57] X. Deng, X. Gan, and M. Gu. Multiphoton fluorescence microscopic imaging through double-layer turbid tissue media. J. Appl. Phy., 91:4659:4665, 2002.

[58] P. A. Franken, A. E. Hill, C. W. Peters, and G. Weinreich. Generation of optical harmonics. Phys. Rev. Lett., 7:118:120, 1961.

[59] R. W. Terhune, P. D. Maker, and C. M. Savage. Optical harmonic generation in calcite. Phys. Rev. Lett., 8:404:406, 1962. 150 Bibliography

[60] R. Hellwarth and P. Christensen. Nonlinear optical microscopic examination of structure in polycrystalline znse. Opt. Communication, 12:318:322, 1974.

[61] Freund and M. Deutsch. Second-harmonic microscopy of biological tissue. Opt. Lett., 11:94:96, 1986.

[62] Y. Guo, P. P. Ho, H. Savage, D. Harris, P. Sacks, S. Schantz, F. Liu, N. Zhadin, and R. R. Alfano. Optical harmonic generation from animal tissue by the use of picosecond and femtosecond laser pulses. Opt. Lett., 22:1323:1325, 1997.

[63] R. Gauderon, P. B. Lukins, and C. J. R. Sheppard. Three-dimensional secondharmonic generation imaging with femtosecond laser pulses. Opt. Lett., 23:1209:1211, 1998.

[64] L. Moreaux, O. Sandre, S. Charpak, M. Blanchard-Desce, and J. Mertz. Coherent scattering in multi-harmonic light microscopy. Biophys. J., 80:1568:1574, 2001.

[65] D. A. Dombeck, K. A. Kasischke, H. D. Vishwasrao, M. Ingelsson, B. T. Hyman, and W. W. Webb. Uniform polarity microtubule assemblies imaged in native brain tissue by second-harmonic generation microscopy. Proc. Natl. Acad. Sci. USA, 100:7081:7086, 2003.

[66] Y. Barad, H. Eizenberg, M. Horowitz, and Y. Silberberg. Nonlinear scanning laser microscopy by third-harmonic generation. Appl. Phys. Lett., 70:922:924, 1997.

[67] A. Squier, M. Muller, G. J. Brakenhoff, and K. R. Wilson. Third harmonic generation microscopy. Opt. Express, 3:315:324, 1998.

[68] D. Yelin and Y. Silberberg. Laser scanning third-harmonic-generation microscopy in biology. Opt. Express, 5:169:175, 1999.

[69] S. Chu, I. Chen, T. Liu, P. C. Chen, and C. Sun. Multimodal nonlinear spectral microscopy based on a femtosecond Cr:Forsterite laser. Opt. Lett., 26:1909:1911, 2001. 151 Bibliography

[70] P. Stoller, K. M. Reiser, P. M. Celliers, and A. M. Rubenchik. Polarization modulated second harmonic generation in collagen. Biophys. J., 82:3330:3342, 2002.

[71] P. Stoller, B. M. Kim, A. M. Rubenchik, K. M. Reiser, and L. B. D. Silva. Polarization-dependent optical second-harmonic imaging of a rat-tail tendon. J. Biomed. Opt., 7:205:214, 2002.

[72] T. Yasui, Y. Tohno, and T. Araki. Determination of collagen fiber orientation in human tissue by use of polarization measurement of molecular second-harmonic generation light. Appl. Opt., 43:2861:2867, 2004.

[73] S. W. Chu, S. Y. Chen, G. W. Chern, T. H. Tsai, Y. C. Chen, B. L. Lin, and C. K. Sun. Studies of _(2)/_(3) tensors in submicron-scaled bio-tissues by polarization harmonics optical microscopy. Biophys. J., 86:3914:3922, 2004.

[74] X. Deng, E. D. Williams, E. W. Thompson, X. Gan, and M. Gu. Second-harmonic generation from biological tissues: Effect of excitation wavelength. Scanning, 24:175:178, 2002.

[75] S. Fine and W. P. Hansen. Optical second harmonic generation in biological systems. Appl. Opt., 10:2350:2353, 1971.

[76] Moreaux, O. Sandre, and J. Mertz. Membrane imaging by second-harmonic generation microscopy. J. Opt. Soc. Am. B, 17:1685:1694, 2000.

[77] Moreaux, T. Pons, V. Dambrin, M. Blanchard-Desce, and J. Mertz. Electro optic response of second-harmonic generation membrane potential sensors. Opt. Lett., 28:625:627, 2003.

[78] C. Millard, L. Jin, A. Lewis, and L. M. Loew. Direct measurement of the voltage sensitivity of second-harmonic generation from a membrane dye in patch clamped cells. Opt. Lett., 28:1221:1223, 2003. 152 Bibliography

[79] C. Millard, L. Jin, M.Wei, J. P.Wuskell, A. Lewis, and L. M. Loew. Sensitivity of second harmonic generation from styryl dyes to transmembrane potential. Biophys. J., 86:1169:1176, 2004.

[80] Sun, S. Chu, S. Chen, T. Tsai, T. Liu, C. Lin, H. Tsai. Higher harmonic generation microscopy for developmental biology. Journal of Structural Biology, 147:19:30, 2004.

[81] R. M. Williams, W. R. Zipfel, and W. W. Webb. Interpreting second-harmonic generation images of collagen I fibrils. Biophys. J., 88:1377:1386, 2005.

[82] E. Brown, T. McKee, E. di Tomaso, A. Pluen, B. Seed, Y. Boucher, and R. K. Jain. Dynamic imaging of collagen and its modulation in tumors in vivo using second-harmonic generation. Nat. Medicine, 9:796:800, 2003.

[83] P. D. Maker and R. W. Terhune. Study of optical effects due to an induced polarization third order in the electric field strength. Phys. Rev., 137:A801 :A818, 1965.

[84] L. Evans, E. O. Potma, M. Puoris'haag, D. Cote, C. P. Lin, and X. S. Xie. Chemical imaging of tissue in vivo with video-rate coherent

anti-stokes Raman scattering microscopy. Proc. Natl. Acad. Sci. USA, 102:16807:16812, 2005.

[85] Kano and H. Hamaguchi. In vivo multi-nonlinear optical imaging of a living cell using a supercontinuum light source generated from a photonic crystal fibre. Opt. Express, 14:2798:2804, 2006.

[86] A W Snyder and J D Love, Optical Waveguide Theory (Chapman & Hall, 1983).

[87] K Y Lau. Propagation path length variations due to bending of optical fibers. Telecommun. Data Acquisition Progress Report, NASA/Jet Propulsion Laboratory, Pasadena, CA, USA, 42-63(Mar./Apr.):26-32, 1981.